IMPACT OF NANOSECOND LASER ENERGY DENSITY ON THE C40-TiSi2 FORMATION AND C54-TiSi2 TRANSFORMATION TEMPERATURE.

Laura Esposito, S. Kerdiles, M. Gregoire, P. Benigni, K. Dabertrand, Jean-Gabriel Mattei, D. Mangelinck

Journal of Applied Physics

IMPACT OF NANOSECOND LASER ENERGY DENSITY ON THE C40-$TiSi_2$ FORMATION AND C54-$TiSi_2$ TRANSFORMATION TEMPERATURE.

L. Esposito[1,2,3,a)], S. Kerdilès[2], M. Gregoire[1], P. Benigni[3], K. Dabertrand[1], J.-G. Mattei[1] and D. Mangelinck[3]

[1]*STMicroelectronics, 850, rue Jean Monnet, 38926, Crolles cedex, France*

[2]*Université Grenoble Alpes, CEA-LETI, F-38000 Grenoble, France*

[3]*Laboratoire Matériaux et Microélectronique de Provence, L2MP-UMR CNRS 6137, Case 142, Faculté de Saint Jérôme, 13397 Marseille Cedex 20, France*

[a)] Author to whom correspondence should be addressed to: laura.esposito@im2np.fr

ABSTRACT

The formation of Ti based contacts in new image sensors CMOS technologies is limited by the requirement of low thermal budget. The objectives for these new 3D-technologies are to promote ohmic, low resistance, repeatable and reliable contacts by keeping the process temperature as low as possible. In this work, UV-nanosecond laser annealing were performed before classical rapid thermal annealing (RTA) to promote the formation at lower RTA temperatures of the low resistivity C54-$TiSi_2$ phase. The laser energy density was varied from 0.30 to 1.00 J/cm² with 3 pulses in order to form the C40-$TiSi_2$ phase and finally to obtain the C54-$TiSi_2$ phase by a subsequent RTA at low temperature. The formed Ti-silicides were characterized by four-point probe measurements, X-Ray Diffraction, Transmission Electron Microscopy and Atom Probe Tomography. A threshold in the laser energy density for the formation of the C40-$TiSi_2$ is observed at an energy density of 0.85 J/cm² for the targeted TiN/Ti stack on blanket wafers. The C40-$TiSi_2$ formation by laser annealing prior to RTA enables to reduce the formation temperature of the C54-$TiSi_2$ phase by 150°C in comparison to a single RTA applied after the Ti/TiN deposition. This specific phase sequence is only observed for a laser energy density close to 0.85 J/cm². At higher energy densities, the presence of C49-$TiSi_2$ or a mix of C49-$TiSi_2$ and C54-$TiSi_2$ is observed. The underlying mechanisms for the phase sequence and formation are discussed in details.

I. INTRODUCTION

As devices sizes are aggressively scaled, the NiPt silicides are widely present in planar technologies[1]. However, they have been replaced by Ti-based silicides in recent contacts for 3D FinFETs (Fin-type Field Effect Transistor) technologies and image sensor CMOS technologies in order to achieve a very low Resistance Capacitance (RC) delay values and high device performances[2–6]. After usual Rapid Thermal Annealing (RTA) in the 550-950°C temperature range, two phases of titanium disilicides ($TiSi_2$) could exist. The high resistivity metastable phase, C49-$TiSi_2$ (60-70 μΩ.cm) is the first phase to grow at a temperature between 550 and 700°C[7,8]. The stable phase, C54-$TiSi_2$, with a low resistivity (15-20 μΩ.cm), is formed from C49-$TiSi_2$ at higher temperatures between 700 and 850°C[7,9–11]. For advanced imagers technologies as well as 3D FinFETs, $TiSi_2$ contacts are formed through the "salicide last" process with a single-step RTA at high temperature without any selective etch of the unreacted Ti layer[12,13]. This is different from the "salicide first" process which implies two RTA (the first one at low temperature and the second at high temperature) with a selective etch of the unreacted metal between the two RTA steps[7]. However, the C49-C54 transformation is difficult in narrow lines because of the nucleation-controlled mechanism which occurs at triple grains boundaries in the C49-$TiSi_2$ phase[14–16]. Indeed, in narrow lines, much fewer nucleation sites are available within the C49-$TiSi_2$ phase. Thus, the thermal budget needs to be increased. Nevertheless, for advanced imagers technologies, the formation temperature of the low resistivity phase is too high to enable co-integration with other silicides such as NiSi. Particularly, NiSi is prone to agglomeration at around 600°C and above, depending on its thickness, the alloying elements and the annealing conditions[17–20]. To extend the use of $TiSi_2$, several groups have been working on the decrease of the thermal budget required to obtain the C54-$TiSi_2$ phase. Various methods were employed such as pre-amorphizing implantation of Si by Ge[4,21–23], As[22,24,25] or Sb[22,26] ions as well as the use of refractory metals either as interlayer or as alloying elements[27–29]. Pulsed laser annealing has also been investigated and several important benefits have been demonstrated. First, due to its fast ramping rate and short anneal duration, nanosecond laser annealing (UV-NLA) has been found to enable the formation of smaller grains of C49-$TiSi_2$ than RTA[30–32], increasing the density of C54-$TiSi_2$ nucleation sites. Chen et al.[30] have also reported that the transformation temperature into C54-$TiSi_2$ can be significantly reduced by pulsed laser annealing. Moreover, the technologically favorable C54-$TiSi_2$ phase has been obtained directly after the laser annealing step[30,32,33]. Another major interest of the laser annealing process is to modify the phase sequence: indeed the C54-$TiSi_2$ phase can be obtained from C40-$TiSi_2$, by-passing the undesirable C49-$TiSi_2$ phase[34–36]. The C40-$TiSi_2$ phase, obtained for very specific conditions, can thus act as a precursor of the C54-$TiSi_2$ at lower temperature[34–36]. The

investigation performed so far on leveraging UV-NLA for the formation of $TiSi_2$ have been mainly conducted with small laser beams (diameter ~160-200 µm) with a near Gaussian shape scanning the surface with a controlled speed, resulting in a large number of pulses at the same location (typically more than 100 pulses)[30–36]. Such studies did not properly explore the effect of the laser energy density.

In the present paper, leveraging a large laser beam with a top hat intensity profile and an accurate energy density control, the impact of the UV-NLA energy density on the formation of the C54-$TiSi_2$ is investigated and compared to numerical simulations. In our case, the starting Ti film thicknesses are three times thinner than in the previous published works, in order to match with the requirements for contacts in state of the art imaging technologies. The different phases formed with various laser processing conditions were analyzed by several characterization techniques. Finally, the different sequences of silicide formation are discussed in terms of thermodynamics, nucleation and kinetics.

II. EXPERIMENTS

300 mm diameter p-type <100> silicon wafers were used as starting materials in the present study. Theses substrates were at first submitted to a wet surface preparation including a diluted HF solution and then a SC1 solution ($NH_4OH/H_2O_2/H_2O$) to generate a controlled surface oxide layer. The cleaned wafers were then loaded in a deposition cluster tool under secondary vacuum where the surface oxide was removed by a SiCoNi™ dry-clean (the chemical oxide is transformed into a salt by a NH_3/NF_3 remote plasma which is sublimated at a temperature lower than 180°C, typically). Without vacuum break, 10 nm ± 1 nm Ti and 10 ± 1 nm TiN layers were then successively deposited. The samples were then annealed either using only UV-NLA or combining UV-NLA and a subsequent RTA. UV-NLA was performed with a SCREEN LT3100 platform based on a XeCl excimer laser (wavelength: λ=308 nm, Full Width at Half Maximum of the pulse: τ = 160 ns) in N_2 atmosphere. Different 15 x 15 mm² fields (corresponding to the beam size) were irradiated by 3 pulses UV-NLA with increasing laser Energy Density (ED) ranging from 0.3 to 1.0 J/cm² on the same wafer. The laser beam had a "top hat" shape and the beam homogeneity was better than 2.5 % within each field of exposure. The laser is stepped across the wafer, with a change of the ED for each coordinate. Each region annealed by the laser are separated from each other by 3,5 mm. The RTA step was conducted at different temperatures between 550 and 950°C for 30 seconds under N_2 atmosphere using a Levitor4300 system from Levitech. Sheet resistances (Rs) of the samples were measured using a four-point probe NAPSON WS3000 tool. Samples were also characterized by High Resolution Transmission Electron Microscopy / Energy Dispersive X-ray spectrometry

(HRTEM-EDX), Scanning Electron Microscopy (SEM) and Atom Probe Tomography (APT). The Ti-silicide phases formed were identified by X-Ray Diffraction using the θ-θ configuration with 1.541 Å ($Cu\ K_\alpha$) radiation.

III. RESULTS

A. AS DEPOSITED SAMPLE

Fig. 1 presents the TEM micrograph of the as-deposited sample. It can be described with three distinct layers. Above the Si substrate, a 3.0 ± 0.2 nm thick amorphous silicide ($a\text{-}Ti_{1-x}Si_x$) is observed and attributed to the intermixing occurring during either the Ti deposition or the subsequent TiN deposition (equivalent to an anneal of 2 minutes at 370°C). On top of this layer, a crystalline and 7 ± 1 nm thick columnar layer of Ti and a similar morphology layer of 8.0 ± 0.5 nm identified as the TiN layer are observed.

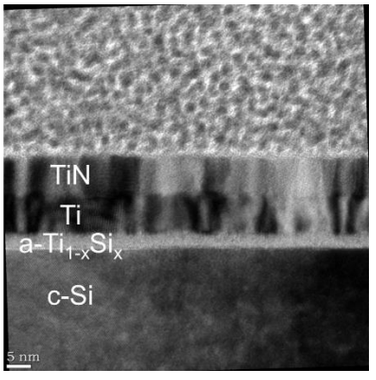

Fig. 1 – TEM micrograph corresponding to the as-deposited sample TiN/Ti/Si. The TiN and Ti target thicknesses were fixed around 10 nm. Three layers are clearly identified as TiN, Ti and $a\text{-}Ti_{1-x}Si_x$ on top of the Si substrate.

B. UV-NLA

The Rs of samples submitted to 3 UV-NLA pulses as a function of laser energy density in the 0.3-1.0 J/cm² range is shown in Fig. 2 (black squares). Four different regimes can be deduced from this curve. Below 0.75 J/cm², Rs remains stable and similar to the post deposition value around 70 Ω/sq (1). Between 0.750 and 0.825 J/cm², the Rs increases up to a maximum of 86 Ω/sq (2). Above 0.825 J/cm², the Rs decreases down to 35 Ω/sq at 0.875 J/cm² (3) and then, more slowly beyond 0.875 J/cm² down to 24 Ω/sq for 1.00 J/cm² (4). Fig. 2 also presents the Rs as a function of laser ED for samples submitted to UV-NLA combined with RTA at 650°C

(red triangles). After UV-NLA followed by RTA at 650°C, the Rs remains stable around 26 Ω/sq for ED between 0.3 and 0.8 J/cm² and then exhibits a sharp minimum around 10 Ω/sq for a laser ED close to 0.85 J/cm². This specific laser processing condition (0.85 J/cm²) corresponds to the middle of the sharp drop of Rs before RTA, with a value around 60 Ω/sq. Above this ED, for both UV-NLA and RTA steps, Rs increases up to 28 Ω/sq for an ED of 0.95 J/cm² and then slowly decreases until 20 Ω/sq for higher ED. The ED leading to the minimum of resistance is thus 0.85 J/cm². Selected samples exhibiting a significant evolution of Rs after UV-NLA were submitted to further characterizations. The results associated to UV-NLA combined to RTA will be discussed in a second part.

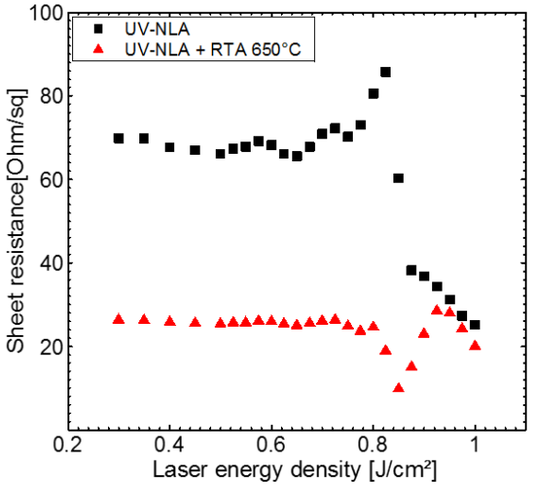

Fig. 2 - Sheet resistance as a function of laser energy density after 3 UV-NLA pulses only (black squares) and UV-NLA followed by RTA at 650°C for 30s (red triangles).

The XRD profiles of the samples annealed with a laser energy density in the 0.75 to 1.00 J/cm² range are displayed in Fig. 3. The XRD profiles show some trends that can be linked to the different regimes identified in the Rs evolution as a function of ED (Fig. 2). For the sample annealed at 0.75 J/cm², the XRD profile is similar to the as-deposited sample profile. Three overlapping peaks are observed and can be identified as TiN, TiO_2 (or $TiNO_x$) and Ti peaks. They have the same intensity before and after UV-NLA. The peak related to oxidized Ti is attributed to TiO_2 but it could also be linked to $TiNO_x$, considering the material stack: TiN/Ti/Si. The TiN capping layer role is to prevent the Ti oxidation. If an oxidation nevertheless occurs upon air exposure (after deposition) or during the anneal, it might result in the oxidation of the TiN layer. With increasing ED in the 0.80-0.90 J/cm² range, the Ti peak progressively disappears indicating Ti consumption. The TiO_2/$TiNO_x$ peak vanishes, suggesting a redistribution of the oxygen in the sample as the ED increases. On the other hand, no

other peaks are detected, suggesting the formation of an amorphous layer in association to the Ti consumption. Above 0.90 J/cm², the TiN peak is still present but there is no more Ti peak in the XRD profile, indicating that Ti is fully consumed during the reaction. Moreover, a second peak appears at 40.52° corresponding to the formation of the C40-$TiSi_2$ phase. This peak has a low intensity probably because of the low thickness and the microstructure of the C40-$TiSi_2$ layer.

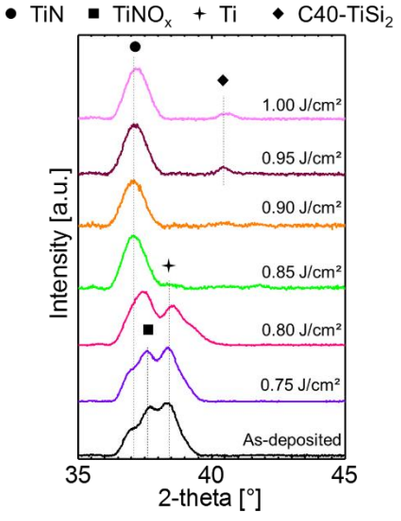

Fig. 3 - θ-θ XRD measurements corresponding to the as-deposited TiN/Ti/Si sample and those annealed with 3 UV-NLA pulses at various energy densities in the 0.75-1.00 J/cm² range. The intensity is normalized to the highest intensity peak.

Samples annealed with 3 UV-NLA pulses at EDs of 0.80 and 0.85 J/cm² were characterized by HRTEM and TEM-EDX. Fig. 4a shows a cross-section HRTEM micrograph of the sample annealed at 0.80 J/cm². The corresponding EDX depth profiles are displayed in Fig. 4b. On top of the Si substrate, three distinct layers can be identified from the bottom to the top: a 5.6 ± 0.2 nm thick a-$Ti_{1-x}Si_x$, a 5.4 ± 0.2 nm thick crystalline Ti layer and another crystalline layer of 9.8 ± 0.3 nm thick, made of columnar TiN. The measured stoichiometry in the TiN is close to 1:1. The EDX depth profile in the a-$Ti_{1-x}Si_x$ layer shows that a composition gradient is present in the silicide layer. Indeed, even if it is difficult to measure the composition of the amorphous phase due to its small thickness, the Si concentration varies approximately from 40 to 65 at. %. The average Ti:Si ratio measurement is close to 1:1 indicating the formation of a silicide with a composition close to TiSi.

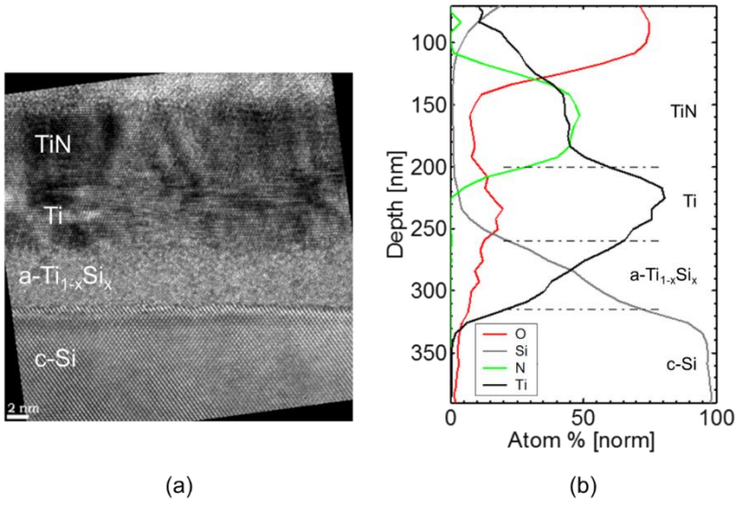

Fig. 4 - (a) HRTEM micrograph corresponding to the sample annealed at 0.80 J/cm² with 3 UV-NLA pulses. Three layers are clearly identified as TiN, Ti and a-$Ti_{1-x}Si_x$ on top of the Si substrate. (b) TEM-EDX depth profiles corresponding to the same sample.

Similar observations have been performed on the sample annealed at 0.85 J/cm². The corresponding HRTEM cross-section micrograph and the EDX depth profiles are shown in Fig. 5a and Fig. 5b respectively. In opposition to the sample annealed at 0.80 J/cm², this sample is made of two distinct layers on top of the Si substrate: a silicide layer with a thickness varying between 17 and 21 ± 0.6 nm, depending on the silicide/Si interface morphology, and a 8.4 ± 0.3 nm-thick columnar and crystalline TiN layer similar to the one observed in the previous figure. The analysis of the electron diffraction pattern during TEM observations (not shown) revealed that the silicide layer was at least partially crystalline. It was however difficult to determine if it is fully crystallized or not. The EDX profile of the sample leads to similar Ti:N ratio of 1:1 for the TiN layer. The average Ti:Si ratio in the silicide layer is found to be close to 1:2 indicating the formation of a silicide close to $TiSi_2$ but not perfectly stoichiometric. Indeed, the Ti and Si EDX depth profiles evidence a composition gradient in the silicide layer, being slightly Si-rich at the silicide/Si interface, compared to $TiSi_2$.

Fig. 6a displays the APT reconstructed volume of the nano-tip fabricated by Focused Ion Beam (FIB) from the same sample annealed at 0.85 J/cm². The reconstructed volume confirmed the presence of three different layers along the tip. The distribution of TiN (green) molecule, Ti (black) and Si (grey) atoms enables to identify the layers from the top to the bottom of the tip as: TiN, Ti-silicide and c-Si. No Ti layer was found between the TiN and the silicide layers, which is in agreement with the corresponding XRD profile and TEM-EDX characterizations. Fig. 6b displays the 1D atomic concentration profile for Ti, Si and N atoms extracted from the

reconstructed volume along the arrow represented in Fig. 6a. The profiles are similar to those obtained by EDX (Fig. 5b) with a TiN composition close to the 1:1 stoichiometry. The depth profiles of Ti and Si also evidence a concentration gradient within the silicide layer with an average composition in agreement with the EDX profile.

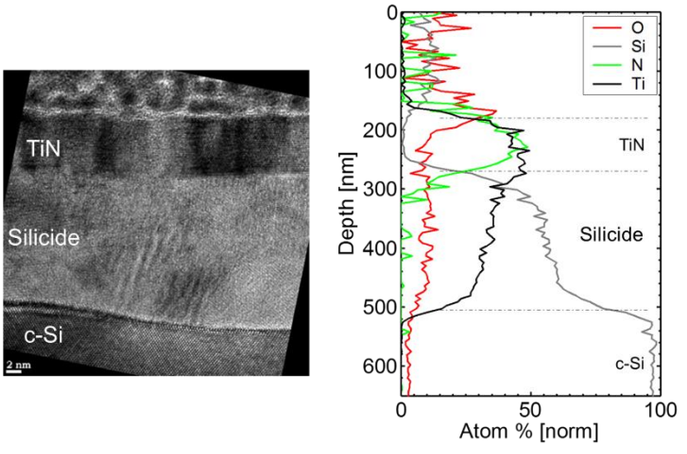

Fig. 5 - (a) HRTEM micrograph corresponding to the sample annealed at 0.85 J/cm² with 3 UV-NLA pulses. TiN and Ti-silicide layers are clearly identified on top of the Si substrate. (b) TEM-EDX depth profiles for the same sample.

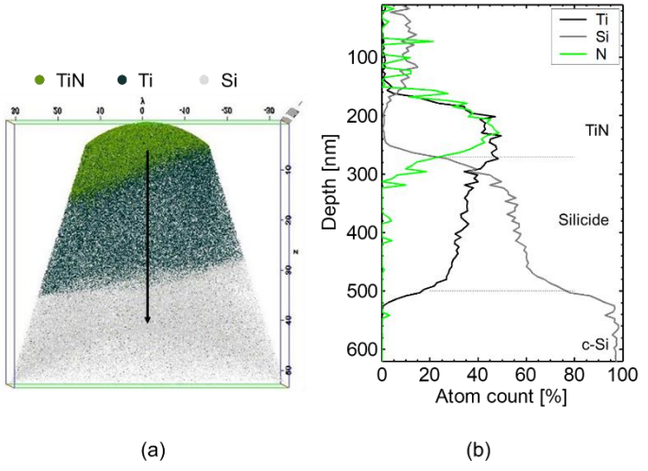

Fig. 6 - APT analysis of the TiN/Ti/Si sample annealed with 3 UV-NLA pulses at 0.85 J/cm². (a) Reconstructed volume showing the top TiN layer, the silicide layer and the Si substrate. (b) Corresponding 1D concentration depth profiles along the tip.

In order to get information of the morphology, SEM top view observations were performed. Fig. 7 displays the corresponding 5x5 µm² collected images after Ti/TiN deposition (Fig. 7a) and after UV-NLA exposure with 3 pulses at various laser energy densities (Fig. 7b-f). At 0.80 J/cm², the surface layer (TiN) remains smooth similarly to the as-deposited samples. From 0.85 J/cm², the samples surface exhibits some periodic ripples, with a period and an amplitude increasing with the laser ED. The characteristic period of these ripples increases from ~25 nm for 0.85 J/cm² up to ~350 nm for 1.00 J/cm². These ripples are at the origin of the curved a-$Ti_{1-x}Si_x$/Si interface observed on HRTEM (Fig. 5a) for the sample annealed at 0.85 J/cm² with 3 UV-NLA pulses.

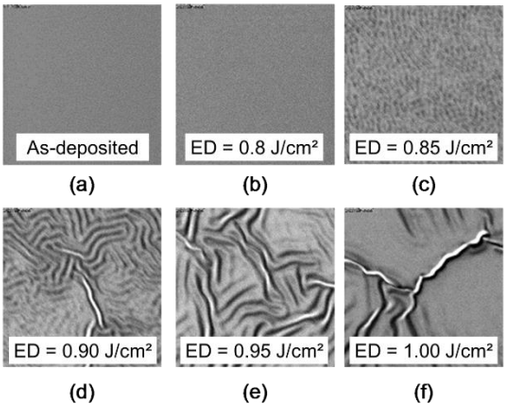

Fig. 7 - 5x5 µm² top-view SEM observations of TiN/Ti/Si samples (a) as-deposited or submitted to 3 UV-NLA pulses with following laser ED : (b) 0.80, (c) 0.85, (d) 0.90, (e) 0.95 and (f) 1.00 J/cm².

C. UV-NLA AND SUBSEQUENT RTA

To estimate the potential benefit of a pre-laser annealing on the C54-$TiSi_2$ formation temperature, a post-thermal treatment of the samples was carried out using RTA in a N_2 ambient. To identify the optimal combination between UV-NLA and RTA process conditions, we measured the sheet resistance of samples first exposed to 3 UV-NLA pulses with ED between 0.3 and 1.0 J/cm² and then RTA at temperatures between 550 and 950°C (for 30 s). Results are plotted in Fig. 8 using a 2D mapping as a function of both RTA temperature and laser ED with a color scale for Rs values ranging from 7 Ω/sq (blue) to 30 Ω/sq (red). For laser EDs from 0.3 to 0.8 J/cm², the Rs evolution is driven by RTA temperature and not by the laser ED. Indeed, Rs decreases from values above 30 Ω/sq to a minimum of 7-9 Ω/sq when RTA temperature increases up to 850°C and then

it increases again up to 30 Ω/sq for RTA temperatures above 900°C. This behavior is similar to the reference sample without UV-NLA prior to RTA (not shown). In the 2D color map, it results in the vertical blue valley, corresponding to a minimum Rs value, in the 7-9 Ω/sq range. For laser ED around 0.85 J/cm², this valley spreads horizontally to include RTA temperature in the 650-800°C range. Above this energy density, an increase of the sheet resistance is observed. The lowest RTA temperature for which the minimum sheet resistance is reached is 650°C.

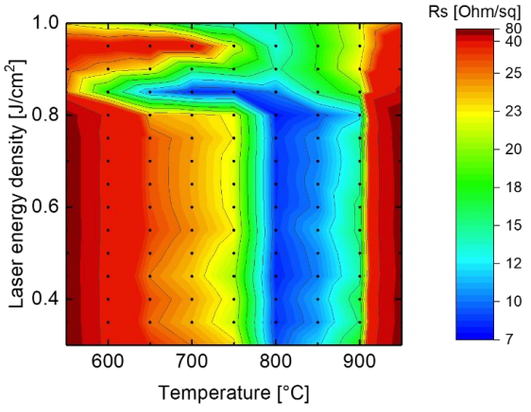

Fig. 8 - 2D color map showing the evolution of Rs for TiN/Ti/Si samples first exposed to 3 UV-NLA pulses at ED in the 0.30-1.00 J/cm² range (Y axis) and submitted to RTA in the 550-900°C range (X axis). Black dots in 2D map are the measured data points.

The phases formed after UV-NLA followed by RTA at 650°C were characterized by θ-θ XRD measurements. The corresponding curves are plotted in Fig. 9. At 0.80 J/cm² and below (not shown), the only detected phase, except TiN, is the C49-$TiSi_2$ one with the (131) peak at 41.1°. At 0.85 J/cm², the only observable phase is the C54-$TiSi_2$ one with a (004) peak at 42.2°. However, XRD profiles corresponding to 0.90 and 0.95 J/cm² show again that only the C49-$TiSi_2$ is detected with the (311) peak and the additional (600) peak at 40.0°. Finally, at 1.00 J/cm², it can be observed that both of C49-$TiSi_2$ and C54-$TiSi_2$ are obtained. Thus, the only process condition for which C54-$TiSi_2$ phase is the only one detected by XRD is 3 laser pulses with a laser energy density of 0.85 J/cm² followed by a RTA at 650°C.

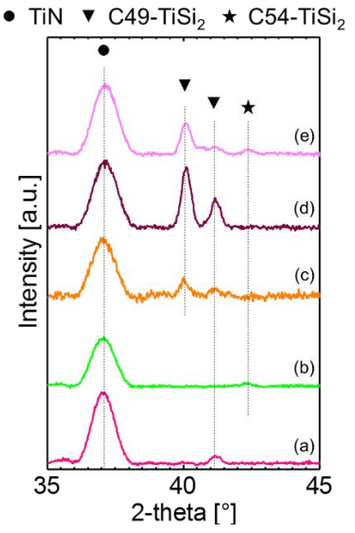

Fig. 9 - θ-θ XRD measurements for TiN/Ti/Si samples annealed with 3 UV-NLA pulses at various energy densities: (a) 0.80, (b) 0.85, (c) 0.90, (d) 0.95 and (d) 1.00 J/cm², followed by RTA at 650°C for 30s. The intensity is normalized to the highest peak.

IV. DISCUSSION

Our results show that different titanium-silicide phases can be obtained depending on the heat treatment conditions (laser ED and RTA temperatures). A summary of the various identified phases is proposed in Fig. 10, in parallel to the sheet resistance evolution of the corresponding samples exposed to UV-NLA only or UV-NLA combined to RTA at 650°C. The phases detected by XRD measurements right after UV-NLA, or after a subsequent RTA at 650°C, are, qualitatively represented by the black or red bars respectively. At EDs below 0.80 J/cm² and RTA temperature below 600°C, the C49-$TiSi_2$ phase is obtained as expected from the typical phase sequences. At the ED of 0.85 J/cm² and RTA temperature of 650°C, the low resistivity C54-$TiSi_2$ is obtained. For higher ED and RTA temperature up to 950°C, either only C49-$TiSi_2$ or a mix of C49-$TiSi_2$ and C54-$TiSi_2$ are observed. The mechanisms of phase formation will be now discussed.

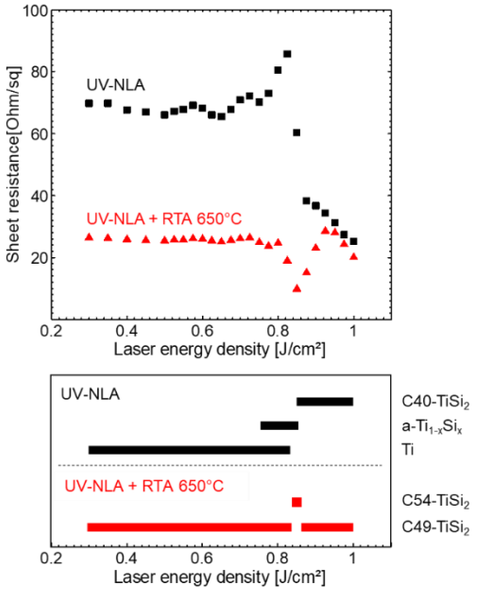

Fig. 10 - Sheet resistance as a function of laser energy density and the phases formed at these ED. Black (after UV-NLA) and red (after UV-NLA followed by a RTA at 650°C) bars qualitatively represent the phases identified in the sample by XRD.

A. NUMERICAL SIMULATIONS OF THE TEMPERATURE DURING UV-NLA

In order to have a better understanding of the physical phenomenon involved during UV-NLA with different ED, 1D numerical simulations have been performed resolving the heat equation coupled to the time-harmonic solution of Maxwell equations[37–39]. Fig. 11 displays the evolution of the calculated surface temperature as a function of time for various laser ED values. The simulated surface temperature corresponds to the temperature obtained in the upper part of the TiN layer in the TiN/Ti/Si stack. Due to the good thermal conductivity of the thin metal films on top of the Si substrate (even after reaction), the surface temperature and the one at the top the Si substrate were found almost equivalent (only around 1% higher for the top surface). For all ED values, the surface temperatures reach a maximum at around t = 190 ns. When increasing ED from 0.70 to 1.00 J/cm², the maximum value of the surface temperature increases from 1200°C to 1540°C. Below 0.80 J/cm², the surface temperatures remain below the Si melting point (1415°C[7]). At 0.80 J/cm², the surface temperature slightly exceeds the temperature of melting of Si, with a temperature around 1428°C. From 0.85 J/cm², the corresponding T = f(time) curves in Fig. 11 exhibit a plateau around 1415°C and a delay in the cooling down of the sample. This change is due to the latent heat that is taken into account during the melting and solidification

of the upper part of the Si substrate. Simulations thus predict the melting of the upper part of the substrate during laser annealing from 0.85 J/cm² and beyond. This is consistent with the SEM top-view observations (shown in Fig. 7) where ripples appear from 0.85 J/cm². Such ripples would be indicative of the presence, for a few nanoseconds during the laser treatment, of a few nanometers of liquid between the upper TiN and the silicon substrate. Benaissa and Moulet[40] claim that the presence of at least 20 nm of liquid between the rigid substrate and a top elastic solid film promotes the stress relaxation of the latter by deformation of both the elastic layer and the liquid foundation, resulting in wrinkles formation. In our case, the liquid phase should correspond to liquid Si. It may also include titanium silicide whose amorphous melting point could be similar or even lower than the Si melting point. In agreement with the theory of wrinkling developed by Huang[41] the characteristic wavelength of the ripples increases with the liquid thickness, *i.e.* with the laser ED in our case, from 25 nm for 0.85 J/cm² to 350 nm for 1.00 J/cm².

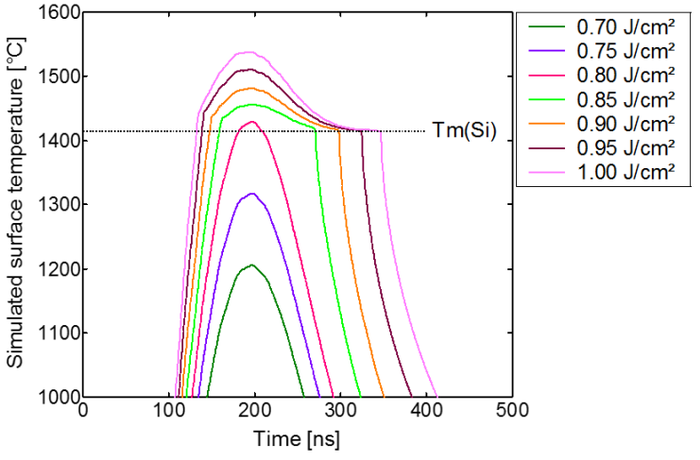

Fig. 11 - Simulated surface temperature as a function of time for laser energy density values from 0.70 to 1.00 J/cm² for 1 pulse.

B. UV-NLA WITHOUT MELTING: GROWTH OF THE AMORPHOUS TI SILICIDE

For 3 pulses UV-NLA with energy densities up to 0.75 J/cm², neither sheet resistance nor XRD profiles (Fig. 2 and Fig. 3 respectively) evidenced any change compared to the as-deposited sample. It can be thus be assumed that UV-NLA did not cause any significant change in the initial TiN/Ti/Si stack in this ED range, even if the sample surface temperature reached up to 1300°C according to our simulations (Fig. 11). However, the increase of the resistance up to 86 Ω/sq for ED in the 0.750-0.825 J/cm² range indicates a change in the samples

stack. In Fig. 3, the associated XRD profiles indicate the consumption of Ti but no silicide-related peak, which is compatible with the formation of an amorphous silicide (a-$Ti_{1-x}Si_x$) upon UV-NLA. At 0.80 J/cm², TEM-EDX observations (Fig. 4a and Fig. 4b) confirm the presence of an amorphous silicide with a composition close to TiSi. For a Ti consumption of 3.4 nm (remaining out of the initial 8 nm), a 5.6 nm thick amorphous silicide is obtained, corresponding to a thickness ratio at 0.80 J/cm² close to 1.64. The growth of an amorphous layer as the first silicide is common during the initial stage of interfacial solid-state reactions of thin films on silicon, either during metal layer deposition and/or more likely during processing in the 200-400°C range with conventional heat treatments[42–46]. According to Raaijmaker et al.[47], the growth of a-$Ti_{1-x}Si_x$ is limited to a thickness of 18 nm, independently of the deposited Ti thickness. They indicated that this growth corresponds to a consumption of 10 nm of Ti yielding a ratio of 1.8. The maximum Rs in our study is measured for an ED of 0.825 J/cm². It can be attributed either to the limited thickness growth of the amorphous silicide (by 18 nm) or to the full consumption of the 11 nm of Ti. Thus, the present study shows that nanosecond laser annealing in the solid-state regime of Ti film deposited on Si, follows the same initial phase sequence with the formation of such amorphous Ti silicide layer despite an extremely short pulse duration.

C. UV-NLA WITH MELTING: FORMATION OF THE C40-$TiSi_2$ PHASE

For ED 0.85 J/cm² and higher, the SEM images and the numerical simulations both are in accordance to indicate that a liquid phase is obtained during the laser pulse. Indeed, Fig. 7 shows that from 0.85 J/cm² the top surface morphology starts to change with the formation of ripples coming from solidification of a liquid, as discussed earlier. The simulations indicate that the maximum temperature varies between 1455°C and 1537°C for ED increasing from 0.85 to 1.00 J/cm² (Fig. 11). Moreover, there is only a variation about 30°C between the top of the TiN layer and the top of the Si substrate. Thus, the temperature might therefore be considered as being roughly constant in the material stack. As the maximum temperatures (1455-1537°C) for ED between 0.85 J/cm² and 1.00 J/cm² are much lower than the melting points of Ti (1668°C) and TiN (2950°C), these two phases should remain solid. However, these temperatures are larger than the melting point of Si (1415°C). The temperature at which the a-$Ti_{1-x}Si_x$ is expected to melt should also be lower than the melting points of Si and $TiSi_2$ (1482°C). If a-$Ti_{1-x}Si_x$ is formed before the temperature reaches the melting point of Si, one can thus expect to obtain a liquid for ED below 0.85 J/cm². However, no ripples are observed by SEM measurements for an ED of 0.80 J/cm² (Fig. 7b) corresponding to a simulated maximum temperature of 1428°C. If the observation of

ripples needs thick enough liquid film (around 20 nm[40]), it is possible that a thin layer has melt at this ED and did not give birth to ripples. Whatsoever, our results strongly suggest that Si is the first phase to melt and that the simulation provide an accurate temperature evolution during UV-NLA. This should be the case at least for the ED of 0.85 J/cm² as the maximum temperature was found close to the melting point of Si. For higher ED, as the melting point of $TiSi_2$ is also exceeded, one might have melting not only of the Si but, also of the reaction products ($aTi_{1-x}Si_x$, $TiSi_2$, …).

Therefore, from the ED of 0.85 J/cm², part of sample is melted and should correspond to melted Si as discussed before. From this ED, there is a sharp decrease of the Rs. Although, no XRD peak was observed for 0.85 J/cm², XRD peaks of the C40-$TiSi_2$ phase are obtained for ED larger than 0,85 J/cm². This strongly suggests that the C40-$TiSi_2$ is formed from the liquid. The absence of the C40-$TiSi_2$ phase for UV-NLA with ED below 0.85 J/cm² (i.e. without melting) also suggests that the C40-$TiSi_2$ formation is not occurring by solid state reaction. It can be assumed that the C40-$TiSi_2$ phase is formed during the fast cooling of the liquid Si. This was also suggested by D'Anna et al. for laser annealing of Ti silicide[48] and for other silicides[49]. However, the formation of the C40-$TiSi_2$ remains unclear and further measurements will be needed to precisely understand the formation mechanism. In particular, it is important to understand the microstructure of the intermediate state (i.e. ED = 0.85 J/cm²). Indeed, this intermediate state is the most important for an industrial process since it enables to obtain the low resistivity C54-$TiSi_2$ phase with a subsequent low temperature RTA.

Moreover, the Rs measurements also show that the transformation into the C40-$TiSi_2$ silicide is not complete with an intermediate value between a-$Ti_{1-x}Si_x$ (ED = 0.80 J/cm²) and C40-$TiSi_2$ (ED > 0.85 J/cm²). The XRD profile in Fig. 3 is not showing any silicide peaks for this energy density while the Ti peak has disappeared: this might be due to very low diffracting volume such as small precipitates. Nevertheless, TEM observations (Fig. 5a) show the presence of some silicide crystallites in the silicide layer. Since the C40-$TiSi_2$ is known to be a stoichiometric phase[35,50] as the majority of other C40-$TiSi_2$ structures (WSi_2[51] and $CrSi_2$[51,52], VSi_2[53], $TaSi_2$[54]), the silicide cannot be only composed of the C40-$TiSi_2$ phase. However, the HRTEM micrograph in Fig. 5a does not show an amorphous layer at the silicide interfaces while the composition gradient in the silicide may be in accordance with the presence of an amorphous silicide together with the C40-$TiSi_2$.

These results suggest that the amorphous silicide and the crystalline C40-$TiSi_2$ co-exist for the ED of 0.85 J/cm². It might be possible that only part of the liquid alloy is transformed into C40-$TiSi_2$ while the remaining liquid alloy may become amorphous during cooling down. Another possibility is that the C40-$TiSi_2$ grows at the

expense of the liquid Si and an amorphous layer grown during the first stage of the UV-NLA, i.e. before the melting. Moreover, as a-$Ti_{1-x}Si_x$ should melt at lower temperature than Si, the a-$Ti_{1-x}Si_x$ layer should have melted before C40-$TiSi_2$ appears. Note than in any cases, the formation of C40-$TiSi_2$ involves the formation of a liquid phase. The most probable phase sequence is thus:

$$Ti + Si \rightarrow a\text{-}Ti_{1-x}Si_x\ (s) \rightarrow Ti_{1-x}Si_x\ (l) \rightarrow C40\text{-}TiSi_2 + a\text{-}Ti_{1-x}Si_x \rightarrow C40\text{-}TiSi_2 \qquad \text{Eq. 1}$$

The gradient in composition measured by EDX and APT could also indicate that the amorphous and C40-$TiSi_2$ phases are intermixed. However, even if an amorphous layer has not been observed by TEM, the composition at the silicide/Si interface is close to $TiSi_2$ and suggests that a layer of C40-$TiSi_2$ is present close to Si. One may thus assume that the silicide layer is composed of a C40-$TiSi_2$ layer and an amorphous layer but further analysis is needed to clarify this point.

In order to obtain more information on the phase formation and their electrical properties, simulations of the resistance were performed using the parallel resistance law for several layers:

$$\frac{1}{R} = \sum_{i=1}^{n} \frac{1}{R_i}$$

where $R_i = \rho_i / t_i$ with ρ_i and t_i being the resistivity and the thickness of each layer. This equation is valid for n materials that form a stack of layers with uniform thickness. Fig. 12 displays the experimental (black squares) and simulated (blue triangles) Rs values as a function of laser ED. The resistivity of the different layers used to fit the resistance curve are the following: ρ_{TiN} = 110 µΩ.cm, $\rho_{a\text{-}TiSi}$ = 330 µΩ.cm, ρ_{Ti} = 105 µΩ.cm and $\rho_{C40\text{-}TiSi2}$ = 140 µΩ.cm. The resistance change was fitted in order to respect the conservation of matter. For ED of 0.825 J/cm² (maximum of the resistance), it was assumed that all the Ti layer is consumed to give about 15 nm of a-$Ti_{1-x}Si_x$. This thickness value seems to be lower than the expected one for the reported a-$Ti_{1-x}Si_x$ / Ti thickness ratio of 1.8[47]. In the simulation, the Rs decrease observed from 0.875 to 1.0 J/cm² was not taken into account. Since, for all these ED, XRD profiles (Fig. 3) show clearly that all the Ti has been completely consumed to form crystalline C40-$TiSi_2$, the thickness of C40-$TiSi_2$ should be constant: the decrease in Rs from 0.875 to 1.0 J/cm² should thus be due to a decrease in resistivity of the C40-$TiSi_2$ layer with the increase of the ED. From the lowest sheet resistance of 25.7 Ω/sq at 1.0 J/cm² and an average C40-$TiSi_2$ thickness of 25 nm, the resistivity of the C40-$TiSi_2$ phase, is estimated to be around $\rho_{C40\text{-}TiSi2,1.0}$ = 70 µΩ.cm. The resistivity of C40-$TiSi_2$ is thus decreased by two for 1.0 J/cm². However this last value is still higher than the one measured by Mammoliti et al.[55] (35 µΩ.cm). The difference may be related to the different C40-$TiSi_2$ thicknesses as the Ti

layer used by Mammoliti et al.[55] was 20 nm thick resulting in a C40-$TiSi_2$ thickness twice as large. Indeed a higher resistivity is usually obtained for thinner film and can be related to several effects[56] such as surface and grain boundary scattering, electron mean free path... Moreover, the continuous decrease in C40-$TiSi_2$ resistivity (Fig. 13) can also be due to the modification of the C40-$TiSi_2$ crystallinity if crystal defects can be reduced with the increasing ED.

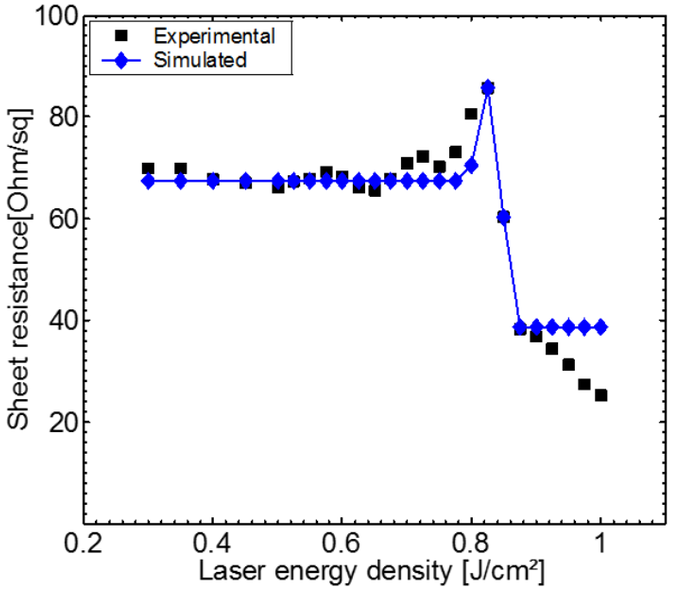

Fig. 12 - Sheet resistance measured by four-point probe measurement (black squares) and simulated (blue triangles) as a function of UV-NLA energy density in the 0.30-1.00 J/cm² (3 pulses).

D. UV-NLA FOLLOWED BY RTA: FORMATION OF C49-$TiSi_2$ AND/OR C54-$TiSi_2$

Neither the C49-$TiSi_2$ nor the C54-$TiSi_2$ phases have been formed with the sole use of the UV-NLA. The only phase formed after UV-NLA is indeed the C40-$TiSi_2$ whatever the laser ED used. To promote the formation of the C54-$TiSi_2$ phase, an additional RTA is needed in agreement with previous studies[34–36,57].

After UV-NLA at ED up to 0.8 J/cm² and a subsequent RTA at 650°C, both XRD (Fig. 9) and Rs measurements (Fig. 2) confirm that the C49-$TiSi_2$ is formed with high sheet resistance values around 27 Ω/sq. This corresponds to the typical phase obtained by RTA at this temperature without UV-NLA, following the classical phase sequences[7,15]. Thus, below a laser ED of 0.80 J/cm², it can be concluded that the laser annealing does not promote the formation of the C54-$TiSi_2$ at low RTA temperature.

After UV-NLA at 0.85 J/cm² followed by RTA at 650°C, the minimal sheet resistance around 7-9 Ω/sq and XRD measurements (Fig. 2 and Fig. 9) both indicate that the expected phase, C54-$TiSi_2$, is obtained and should be the sole silicide present in the sample. In contrast, the formation of the C54-$TiSi_2$ by only RTA needs temperatures up to 800-850°C. Consequently, a UV-NLA + RTA combination enables a decrease of the RTA temperature by more than 150°C compared to the standard RTA approach[58,59]. The sheet resistance and XRD measurements (Fig. 2 and Fig. 9), also show that, for higher ED, a mixture of C49-$TiSi_2$ and C54-$TiSi_2$ is observed. The formation of only C54-$TiSi_2$ with a minimum RTA temperature at 650°C is thus only possible if the UV-NLA results in a mix between a-$Ti_{1-x}Si_x$ and C40-$TiSi_2$ (ED = 0.85 J/cm²).

After UV-NLA at 0.85 J/cm² combined with RTA at 650°C, a C54-$TiSi_2$ layer with a thickness between 17 and 21 nm is obtained. According to Rs simulations (Fig. 12), the C40-$TiSi_2$ thickness after UV-NLA (and before RTA) enabling the formation of C54-$TiSi_2$ only (ED = 0.85 J/cm²) is close to 3 nm. This thickness is significantly lower than the C40-$TiSi_2$ layer thickness determined by Tan et al.[60]. However, they show that the enhancement of the C54-$TiSi_2$ phase from the C40-$TiSi_2$ one is strongly dependent on the thickness of the C40-$TiSi_2$ layer. In their study[60], a thick layer of C40-$TiSi_2$ around 40 nm is undesirable because a higher thermal budget is needed to enable the transformation. On the contrary, a thin layer of C40-$TiSi_2$ (around 15 nm in their case) allows to achieve the C40-C54 transformation at low thermal budget.

In our study, another condition to promote this C40-$TiSi_2$/C54-$TiSi_2$ transformation is obtained. Indeed, it appears that the partial formation of the C40-$TiSi_2$ and/or the presence of amorphous silicide in the layer is a necessary condition to promote the formation of C54-$TiSi_2$ at low RTA temperature. It has been shown that the C40-C54 formation is nucleation controlled[61] with a higher nucleation site density than in the case of C49-C54 transition. Fig. 13 illustrates the different possible nucleation sites of the C54-$TiSi_2$ in two different cases: (a) a partial formation of C40-$TiSi_2$ and (b) a total formation of C40-$TiSi_2$.

Indeed, for a nucleation-controlled reaction, the system must overcome a barrier of nucleation, ΔG^*, given by[62]:

$$\Delta G^* = c\frac{(\Delta\sigma)^3}{(\Delta G_v)^2} \qquad \text{Eq. 2}$$

where $\Delta\sigma$ is the change interfacial energy, ΔG_v the change in volume energy (also called driving force) and c a constant depending on the shape of the critical nucleus.

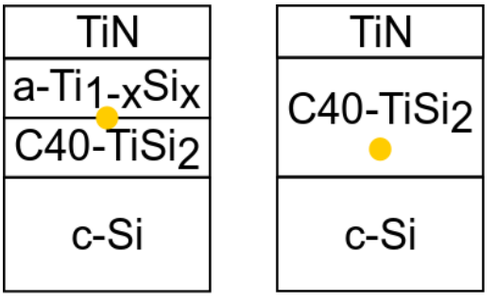

Fig. 13 – Possible nucleation sites of the C54-$TiSi_2$ from the C40-$TiSi_2$. The possible sites are represented by yellow circles in the case of (a) partial formation of C40-$TiSi_2$: a-$Ti_{1-x}Si_x$ and C40-$TiSi_2$ are present on top of Si or (b) total formation of C40-$TiSi_2$: only C40-$TiSi_2$ is present on top of Si.

In order to determine which configuration, *i.e.* (a) partial or (b) total formation of C40-$TiSi_2$, is better to promote the nucleation of C54-$TiSi_2$, the terms $\Delta\sigma$ and ΔG_v in Eq. 2 will now be detailed. It is assumed that the shape of the nucleus is the same in both cases. We further assume that, in case (a) a-$Ti_{1-x}Si_x$ and C40-$TiSi_2$ form continuous layers.

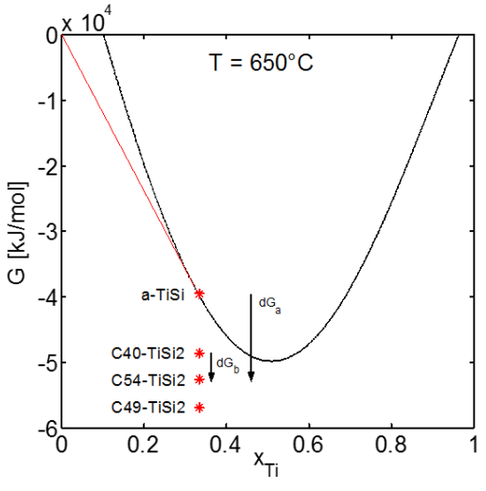

Fig. 14 - Driving force for the nucleation of C54-$TiSi_2$ from the a-$Ti_{1-x}Si_x$ phase (dG_a) and from the C40-$TiSi_2$ phase (dG_b) at 650°C. Red stars correspond from the lowest to the highest value to the Gibbs energies of C49-$TiSi_2$, C54-$TiSi_2$, C40-$TiSi_2$, and a-$Ti_{1-x}Si_x$ with 2/3 of Si respectively.

The nucleation barriers are given in the two cases by:

$$\Delta G_a{}^* = c\frac{(\sigma(C54/C40) + \sigma(C54/a\text{-}Ti_{1-x}Si_x) - \sigma(C40/a\text{-}Ti_{1-x}Si_x))^3}{(\Delta G_v(a\text{-}Ti_{1-x}Si_x \rightarrow C54))^2} \quad \text{Eq. 3}$$

$$\Delta G_b{}^* = c\frac{(\sigma(C54/C40))^3}{(\Delta G_v(C40 \rightarrow C54))^2} \quad \text{Eq. 4}$$

where $\sigma(\alpha/\beta)$ correspond to the energy of the α/β interface and $\Delta G_v(\alpha \rightarrow \beta)$ to the volume energy of the transformation of α into β. The volume energy is related to the driving force, *dG*, through the molecular volume, by $\Delta G_v = dG/\omega$. Fig. 14 shows the Gibbs energies of the different phases in the Ti-Si system and the related driving forces: it is considered as schematic since there are some discrepancies between the relative stability of the C40-$TiSi_2$, C49-$TiSi_2$ and C54-$TiSi_2$ phases in the literature. Indeed, the established Ti-Si phase diagram[7] considers only the C54-$TiSi_2$ phase as being stable. Bonoli et al[63] found by ab initio calculations that the C54-$TiSi_2$ phase is the most stable and that the C49-$TiSi_2$ and C40-$TiSi_2$ phases are less stable with a similar energy about 0.05 eV/atom above the C54-$TiSi_2$. However, in thin films reaction, the metastable C49-$TiSi_2$ phase has been reported for annealing between 550 and 750°C. This behavior can be a consequence of a faster kinetics of formation as often observed in thin films. However, Colinet et al.[64] reported ab-initio calculations where the C49-$TiSi_2$ phase is the most stable phase at temperature lower than 830°C while the C54-$TiSi_2$ phase becomes more stable above this temperature: the C40-$TiSi_2$ being less stable than the C49-$TiSi_2$ and C54-$TiSi_2$ phases. Despite these discrepancies, the a-$Ti_{1-x}Si_x$ phase should be less stable than the C40-$TiSi_2$ that is itself less stable than the C49-$TiSi_2$ and C54-$TiSi_2$ phases. As this corresponds to thin film observations, we used the results from Colinet et al.[64] that give the following order for the Gibbs energies at 650°C (Fig. 14): G(C49-$TiSi_2$) < G(C54-$TiSi_2$) < G(C40-$TiSi_2$) < G(a-$Ti_{1-x}Si_x$). From the driving force aspect, Fig. 14 shows that the nucleation of C54-$TiSi_2$ from a-$Ti_{1-x}Si_x$ will be preferred over the nucleation from the C40-$TiSi_2$ phase. However, in nucleation, the change in interfacial energies should be also considered. As interfacial energies are usually not known and very difficult to determine, only qualitative guess can be made. Due to structural similarity between the C40-$TiSi_2$ and C54-$TiSi_2$ phases[65], the energy of the C40/C54 interface should be very low, while energies of the a-$Ti_{1-x}Si_x$/C54-$TiSi_2$ and a-$Ti_{1-x}Si_x$/C40-$TiSi_2$ interfaces should be relatively large but similar. Note that the C40-$TiSi_2$/C40-$TiSi_2$ interfacial energy is null. The change of interfacial energy should thus be similar for case (a) and (b). Since the driving force, dG_a, is larger than dG_b and the change in interfacial energy is similar, the nucleation barrier for case (a) should be smaller than the nucleation barrier for case (b). The nucleation of the C54-$TiSi_2$ is thus expected to be easier when the formation of C40-$TiSi_2$ is partial than when it is total. Note that for nucleation, a kinetic term should be taken into account in addition to the

nucleation barrier. While for case (b), no change in composition is needed, the diffusion of Si through the C40-$TiSi_2$ phase may be required for case (a) since a-$Ti_{1-x}Si_x$ may not be at the $TiSi_2$ composition. However, this should not limit nucleation since the diffusion of Si should be fast at this temperature. A similar conclusion was reached by Chen et al.[35] who state that the nucleation barrier of the C40-C54 phase transition is higher than the one for the diffusion of Si through C40-$TiSi_2$ layer and formation of C54-$TiSi_2$ on the C40-$TiSi_2$ template layer. In their study[35], the C40-$TiSi_2$ phase was in contact with Ti and not a-$Ti_{1-x}Si_x$ and thus the Si diffusion is mandatory. A similar conclusion can be reached for our study.

In summary, the partial formation of C40-$TiSi_2$ after UV-NLA at 0.85 J/cm² enables an easier nucleation of C54-$TiSi_2$ during the subsequent RTA from the a-$Ti_{1-x}Si_x$ at the a-$Ti_{1-x}Si_x$/C40-$TiSi_2$ interface: this is mainly due to a higher driving force and the template effect of the C40-$TiSi_2$.

For UV-NLA with ED higher than 0.85 J/cm² and RTA at 650°C, the C54-$TiSi_2$ is not the only phase to form. Indeed, the XRD profiles (Fig. 9) show that either C49-$TiSi_2$ or a mix between C49-$TiSi_2$ and C54-$TiSi_2$ is formed at high laser ED. Before RTA, the TEM analysis (not shown) and Rs measurements (Fig. 2) agreed to show that only the C40-$TiSi_2$ phase is obtained (no amorphous layer is present) after UV-NLA with ED higher than 0.85 J/cm². In order to understand these results, it is interesting to look again at the nucleation barrier to compare the nucleation of C49-$TiSi_2$ and C54-$TiSi_2$ from C40-$TiSi_2$. The nucleation barrier for the C40-C49 and C40-C54 transformations can be expressed as:

$$\Delta G_c^* = c\frac{(\sigma(C49/C40))^3}{(\Delta G_v(C40 \rightarrow C49))^2} \quad \text{Eq. 5}$$

$$\Delta G_d^* = c\frac{(\sigma(C54/C40))^3}{(\Delta G_v(C40 \rightarrow C54))^2} \quad \text{Eq. 6}$$

As the C49-$TiSi_2$ is observed experimentally together with C54-$TiSi_2$, the nucleation barrier should be comparable for both nucleation. As σ(C54/C40) is lower than σ(C49/C40), this means that the C49-$TiSi_2$ phase should be more stable than the C54-$TiSi_2$ one at low temperature in line with the ab-initio simulations by Colinet et al[64]. This does not consider the kinetics aspects of nucleation, but no change in composition is involved during the transformation of these disilicides. Even if the growth kinetic could play some role in the phase selection, the nucleation as a necessary first step during the phase formation. For the Ti disilicides formation, it appears that the nucleation is the limiting, and thus the controlling, mechanism. This could be related to the relatively low driving force associated the transition between this phase with the same composition.

These explanations are crucial to understand and control how to obtain low resistance contacts for advanced imagers technology. Indeed, the low resistivity C54-$TiSi_2$ should be formed alone at low temperature to reach this goal and it appears that this requires a complex combination of phase formation from the liquid and nucleation in the solid state. Such a combination can be obtained through UV-NLA and subsequent RTA but only with a reduced process window. To possibly enlarge this process window and to control the molten depth in view of a reproducible process, we could leverage a pre-amorphization implantation that would generate a thin and repeatable amorphous Si layer with a significantly lower melting point at the Ti/Si interface. Ripples observed in case of blanket layers in melt conditions are not expected in case of surfaces with nanometric patterns. For example, in case of contact to be established in the bottom part of a trench, TiN layer should be stabilized by the edges of the trench and avoid the formation of detrimental topology. Besides extra experimental tests, the process window may be improved also by a better understanding of the underlying mechanism such as the silicide formation from the liquid state, the template effect of the C40-$TiSi_2$, the nucleation, kinetics and thermodynamics.

V. CONCLUSIONS

The formation of Ti silicide using UV-NLA and/or RTA has been studied by Rs, XRD, TEM and APT. Different silicides have been obtained depending on the UV-NLA energy densities and the RTA temperatures. The results clearly show that the formation of C40-$TiSi_2$ during UV-NLA enables to enhance the formation of the C54-$TiSi_2$ by subsequent RTA and reduce significantly (from 800 to 650°C) the formation temperature of the C54-$TiSi_2$ phase needed for contacts. There is a threshold in the laser energy density (at 0.85 J/cm²) from which the formation of the C40-$TiSi_2$ becomes possible. Below this threshold, an amorphous silicide grows by solid state reaction in accordance with previous studies that were done at much lower temperature than the ones reached during UV-NLA. The threshold appears to be linked to the melting of Si and the formation of the C40-$TiSi_2$ from the liquid phase. Above the threshold, only the C40-$TiSi_2$ phase is obtained. However, the formation of only C54-$TiSi_2$ at low RTA temperature (650°C) is only possible for one laser energy density (0.85 J/cm²). The proposed mechanism is the following: below the threshold of 0.85 J/cm², no C40-$TiSi_2$ is formed and the transformation into C54-$TiSi_2$ is not possible at a RTA temperature lower than the standard one of 800°C. Above 0.85 J/cm², the Ti layer is fully transformed into C40-$TiSi_2$ and this doesn't allow the total transformation into the C54-$TiSi_2$ under low RTA temperature. At the threshold energy density of 0.85 J/cm², a

mix between C40-$TiSi_2$ and amorphous silicide is obtained and enables an easier nucleation of C54-$TiSi_2$ at the low RTA temperature of 650°C by a template effect of the C40-$TiSi_2$ phase and a high driving force for nucleation. The mechanisms of phase formation are discussed in order to provide a better understanding of the conditions needed to obtain low resistance contact for advanced imagers technologies and 3D FinFET.

SUPPLEMENTARY MATERIAL

See supplementary material for the details of the 1D numerical simulations of the temperature during UV-NLA.

ACKNOWLEDGEMENTS

SCREEN company and its french subsidiary LASSE are gratefully acknowledged for their support in operating and maintaining the LT-3100 nanosecond laser annealing platform. Dominique Mangelinck acknowledges Benoit Appolaire and Myriam Dumont for discussion on phase transformation. Marion Descoins and Maxime Bertoglio are acknowledged for their help on APT and XRD measurements.

AIP PUBLISHING DATA SHARING POLICY

The data that support the findings of this study are available from the corresponding author upon reasonable request.

REFERENCES

[1] Z. Zhang, S.O. Koswatta, S.W. Bedell, A. Baraskar, M. Guillorn, S.U. Engelmann, Y. Zhu, J. Gonsalves, A. Pyzyna, M. Hopstaken, C. Witt, L. Yang, F. Liu, J. Newbury, W. Song, C. Cabral, M. Lofaro, A.S. Ozcan, M. Raymond, C. Lavoie, J.W. Sleight, K.P. Rodbell, and P.M. Solomon, IEEE Electron Device Lett. **34**, 723 (2013).

[2] P. Adusumilli, A. V. Carr, A.S. Ozcan, C. Lavoie, J. Jordan-Sweet, D. Prater, N. Breil, S. Polvino, M. Raymond, D. Deniz, and V. Kamineni, 2016 IEEE Int. Interconnect Technol. Conf. / Adv. Met. Conf. IITC/AMC 2016 139 (2016).

[3] S.A. Chew, H. Yu, M. Schaekers, S. Demuynck, G. Mannaert, E. Kunnen, E. Rosseel, A. Hikavyy, A. Dangol, K. De Meyer, D. Mocuta, N. Horiguchi, G. Leusink, C. Wajda, T. Hakamata, T. Hasegawa, K. Tapily, and R. Clark, IITC 2017 - 2017 IEEE Int. Interconnect Technol. Conf. 5 (2017).

[4] C.P. Chou, C.Y. Chen, K.Y. Chen, S.C. Teng, J.H. Huang, and Y.H. Wu, IEEE Electron Device Lett. **38**, 299 (2017).

[5] R.A. Roy, C. Cabral Jr., and C. Lavoie, Mater. Res. Soc. Symp. Proc. **564**, 35 (1999).

[6] M. Grégoire, B. Horvat, B.N. Bozon, D. Combe, K. Dabertrand, and D. Roy, Micro Nano Eng. 2 104 (2019).

[7] K. Maex, Mater. Sci. Eng. R **11**, 7 (1993).

[8] Z. Ma, Y. Xu, L.H. Allen, and S. Lee, J. Appl. Phys. **74**, 2954 (1993).

[9] A. Mouroux and S.L. Zhang, J. Appl. Phys. **86**, 704 (1999).

[10] L.A. Clevenger and R.W. Mann, J. Electrochem. Soc. **141**, 1347 (1994).

[11] Z. Ma, L.H. Allen, and D.D.J. Allman, J. Appl. Phys. **77**, 4384 (1995).

[12] C. Lavoie, P. Adusumilli, A. V. Carr, J.S. Jordan Sweet, A.S. Ozcan, E. Levrau, N. Breil, and E. Alptekin, ECS Trans. **77**, 59 (2017).

[13] S. Mao and J. Luo, J. Phys. D. Appl. Phys. **52**, (2019).

[14] Z. Ma and L.H. Allen, Phys. Rev. **49**, (1994).

[15] L.J. Chen, *Silicide Technology for Integrated Circuits* (Iet, 2004).

[16] S.-L. Zhang and U. Smith, J. Vac. Sci. Technol. A Vacuum, Surfaces, Film. **22**, 1361 (2004).

[17] D. Mangelinck, J.Y. Dai, J.S. Pan, and S.K. Lahiri, Appl. Phys. Lett. **75**, 1736 (1999).

[18] D. Deduytsche, C. Detavernier, R.L. Van Meirhaeghe, and C. Lavoie, J. Appl. Phys. **98**, (2005).

[19] C. Lavoie, C. Detavernier, C. Cabral, F.M. d'Heurle, A.J. Kellock, J. Jordan-Sweet, and J.M.E. Harper, Microelectron. Eng. **83**, 2042 (2006).

[20] M. Gregoire, R. Beneyton, and P. Morin, IEEE Int. Interconnect Technol. Conf. 2011 Mater. Adv. Met. 1 (2011).

[21] T.C. Hsiao, P. Liu, and J.C.S. Woo, Dig. Tech. Pap. - Symp. VLSI Technol. 95 (1997).

[22] Q. Xu and C. Hu, IEEE Trans. Electron Devices **45**, 2002 (1998).

[23] H. Yu, M. Schaekers, E. Rosseel, A. Peter, J.G. Lee, W.B. Song, S. Demuynck, T. Chiarella, J.A.

Journal of Applied Physics

AIP Publishing

Ragnarsson, S. Kubicek, J. Everaert, N. Horiguchi, K. Barla, D. Kim, N. Collaert, A.V.Y. Thean, and K. De Meyer, Tech. Dig. - Int. Electron Devices Meet. 21.7.1 (2015).

[24] J.U. Bae, D.K. Sohn, J.S. Park, B.H. Lee, C.H. Han, and J.W. Park, J. Appl. Phys. **86**, 4943 (1999).

[25] S.M. Chang, H.Y. Huang, H.Y. Yang, L.J. Chen, C. Appl, P. Lett, S.M. Chang, H.Y. Huang, H.Y. Yang, and L.J. Chen, Appl. Phys. Lett. **224**, (1999).

[26] P. Révész, J. Gyimesi, and É. Zsoldos, J. Appl. Phys. **54**, 1860 (1983).

[27] A. Mouroux, M. Roux, S.L. Zhang, F.M. D'Heurle, C. Cabral, C. Lavoie, and J.M.E. Harper, J. Appl. Phys. **86**, 2323 (1999).

[28] A. Mouroux, S.L. Zhang, W. Kaplan, S. Nygren, M. Östling, and C.S. Petersson, Appl. Phys. Lett. **69**, 975 (1996).

[29] Y.C. Peng, L.J. Chen, W.Y. Hsieh, Y.R. Yang, and Y.F. Hsieh, Appl. Surf. Sci. **142**, 336 (1999).

[30] S.Y. Chen, Z.X. Shen, Z.D. Chen, A.K. See, L.H. Chan, T.J. Zhang, and K.C. Tee, Surf. Interface Anal. **28**, 200 (1999).

[31] Y.F. Chong, K.L. Pey, A.T.S. Wee, A. See, Z.X. Shen, C.H. Tung, R. Gopalakrishnan, and Y.F. Lu, J. Electron. Mater. **30**, 1549 (2001).

[32] S.Y. Chen, Z.X. Shen, Z.D. Chen, L.H. Chan, and A.K. See, Appl. Phys. Lett. **75**, 1727 (1999).

[33] L. Lu and M.O. Lai, J. Appl. Phys. **94**, 4291 (2003).

[34] S.Y. Chen, Z.X. Shen, K. Li, A.K. See, and L.H. Chan, Appl. Phys. Lett. **77**, 4395 (2000).

[35] S.Y. Chen, Z.X. Shen, A.K. See, and L.H. Chan, J. Electrochem. Soc. **148**, 734 (2001).

[36] S.Y. Chen, Z.X. Shen, S.Y. Xu, C.K. Ong, A.K. See, and L.H. Chan, J. Electrochem. Soc. **149**, 609 (2002).

[37] K. Huet, J. Aubin, P.E. Raynal, B. Curvers, A. Verstraete, B. Lespinasse, F. Mazzamuto, A. Sciuto, S.F. Lombardo, A. La Magna, P. Acosta-Alba, L. Dagault, C. Licitra, J.M. Hartmann, and S. Kerdilès, Appl. Surf. Sci. **505**, 144470 (2020).

[38] A. La Magna, P. Alippi, V. Privitera, G. Fortunato, M. Camalleri, and B. Svensson, J. Appl. Phys. **95**, 4806 (2004).

[39] G. Fisicaro and A. La Magna, J. Comput. Electron. **13**, 70 (2014).

[40] L. Benaissa and J.-S. Moulet, US patent N° 10357917 B2 (2019).

[41] R. Huang, J. Mech. Phys. Solids **53**, 63 (2004).

[42] L.A. Clevenger, C. V. Thompson, R.C. Cammarata, and K.N. Tu, Appl. Phys. Lett. **52**, 795 (1988).

[43] L.A. Clevenger and C. V. Thompson, J. Appl. Phys. **67**, 1325 (1990).

[44] M.H. Wang and L.J. Chen, J. Appl. Phys. **71**, 5918 (1992).

[45] T.H. Yang, K.S. Chi, and L.J. Chen, J. Appl. Phys. **98**, (2005).

[46] L.J. Chen, Mater. Sci. Eng. R Reports **29**, 115 (2000).

[47] I.J.M.M. Raaijmakers, A.H. Reader, and P.H. Oosting, J. Appl. Phys. **63**, 2790 (1988).

[48] E.D. Anna, G. Leggieri, A. Luches, M. Martino, A. Peronne, P. Mengucci, and I.N. Mihailescu, Appl. Surf. Sci. **54**, 353 (1992).

[49] E. D'Anna, G. Leggieri, and A. Luches, Appl. Phys. A Solids Surfaces **45**, 325 (1988).

[50] S.C. Tan, A. See, T. Yu, Z.X. Shen, and J. Lin, J. Vac. Sci. Technol. B **480**, (2005).

[51] T.G. Chart, Met. Sci. **9**, 504 (1975).

[52] A.B. Gokhale and G.J. Abbaschian, J. Phase Equilibria **8**, 474 (1987).

[53] C. Milanese, V. Buscaglia, F. Maglia, and U. Anselmi-Tamburini, Acta Mater. **50**, 1393 (2002).

[54] M.E. Schlesinger, J. Phase Equilibria **15**, 90 (1994).

[55] F. Mammoliti, M.G. Grimaldi, and F. La Via, J. Appl. Phys. **92**, 3147 (2002).

[56] W.Zhang, S.H.Brongersma, O.Richard, B.Brijs, R.Palmans, L.Froyen, and K.Maex, Microelectron. Eng. **76**, 146 (2004).

[57] S.Y. Chen, Z.X. Shen, S.Y. Xu, A.K. See, L.H. Chan, and W.S. Li, Mater. Res. Soc. Symp. - Proc. **670**, 2 (2001).

[58] G. Ottaviani, R. Tonini, D. Giubertoni, A. Sabbadini, T. Marangon, G. Queirolo, and F. La Via, Microelectron. Eng. **50**, 153 (2000).

[59] L.A. Clevenger, J.M.E. Harper, C. Cabral, C. Nobili, G. Ottaviani, and R. Mann, J. Appl. Phys. **72**, 4978 (1992).

[60] S.C. Tan, L. Liu, Y.P. Zeng, A. See, and Z.X. Shen, J. Electrochem. Soc. **152**, 754 (2005).

[61] F. La Via, F. Mammoliti, and M.G. Grimaldi, J. Appl. Phys. **91**, 633 (2002).

[62] F.M. d'Heurle, J. Mater. Res. **3**, 167 (1988).

[63] F. Bonoli, M. Iannuzzi, L. Miglio, and V. Meregalli, Appl. Phys. Lett. **73**, 10 (1998).

[64] C. Colinet, W. Wolf, R. Podloucky, A. Pasturel, and W. Wolf, Appl. Phys. Lett. **87**, (2005).

[65] A. Mouroux, T. Epicier, S.L. Zhang, and P. Pinard, Phys. Rev. B - Condens. Matter Mater. Phys. **60**, 9165 (1999).

AIP Publishing

Journal of Applied Physics

ACCEPTED MANUSCRIPT

PLEASE CITE THIS ARTICLE AS DOI: 10.1063/5.0016091

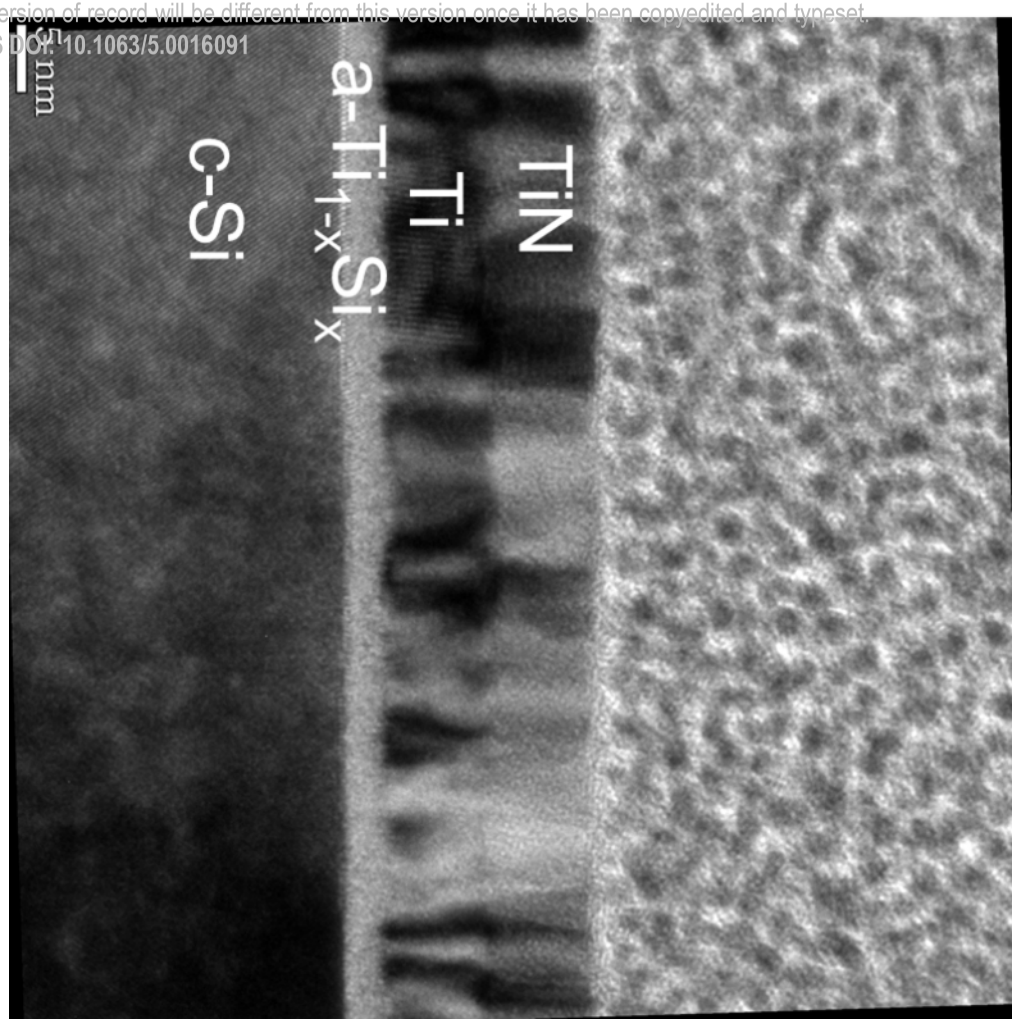

Journal of Applied Physics

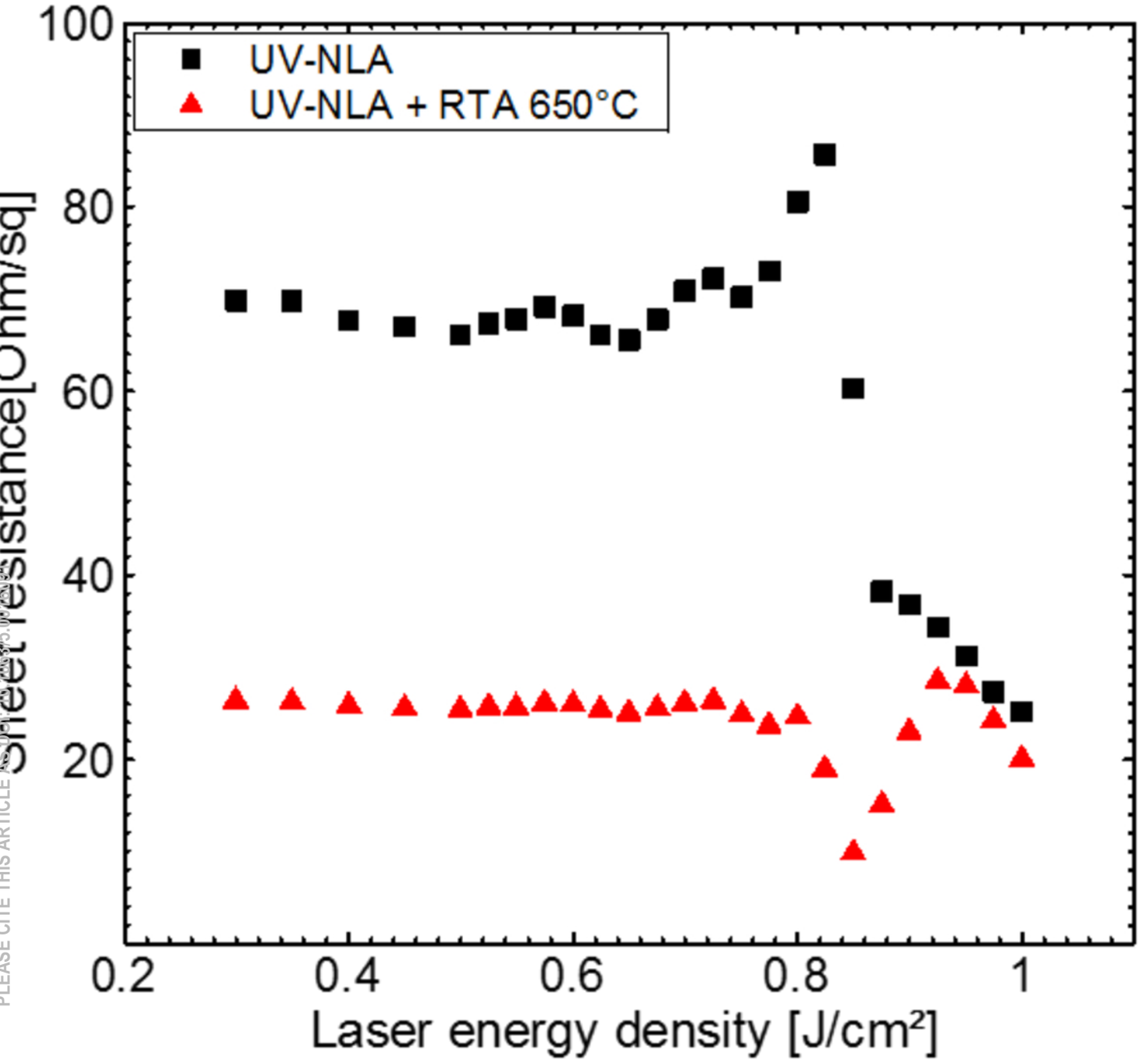

AIP Publishing

Journal of Applied Physics

AIP Publishing

AIP Publishing

Journal of Applied Physics

ACCEPTED MANUSCRIPT

PLEASE CITE THIS ARTICLE AS DOI: 10.1063/5.0016091

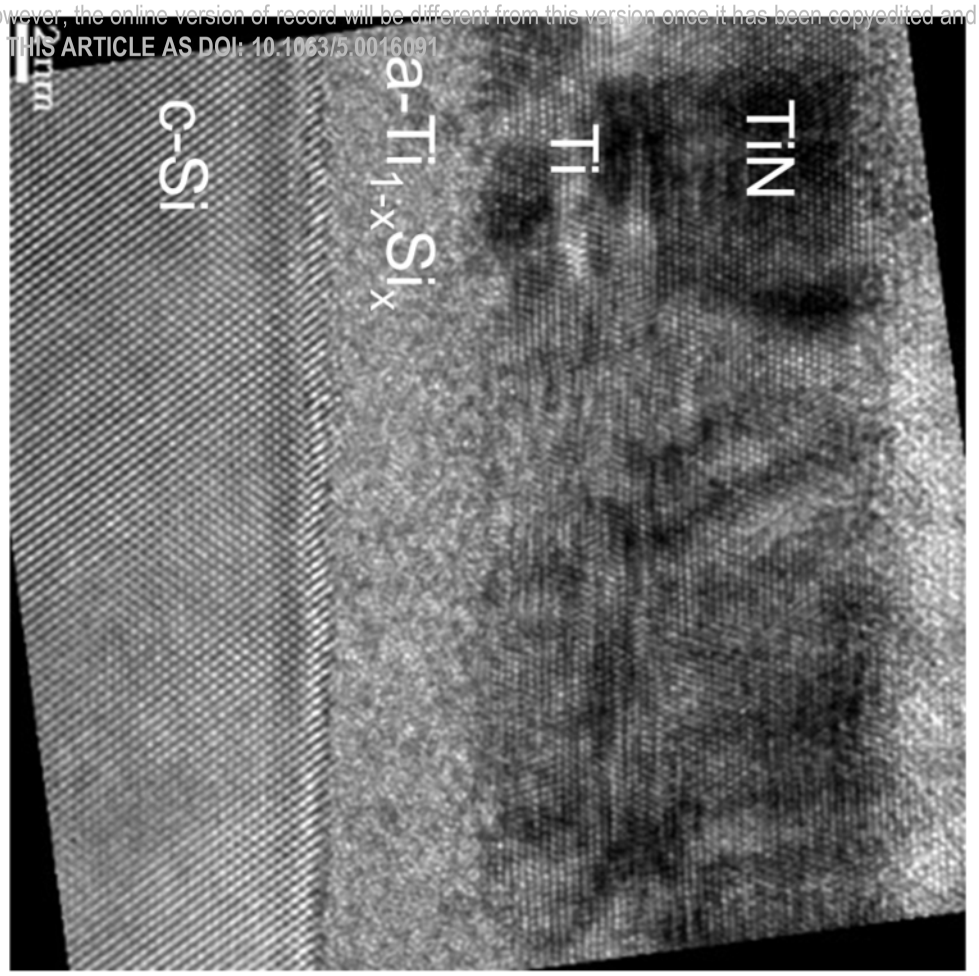

(a)

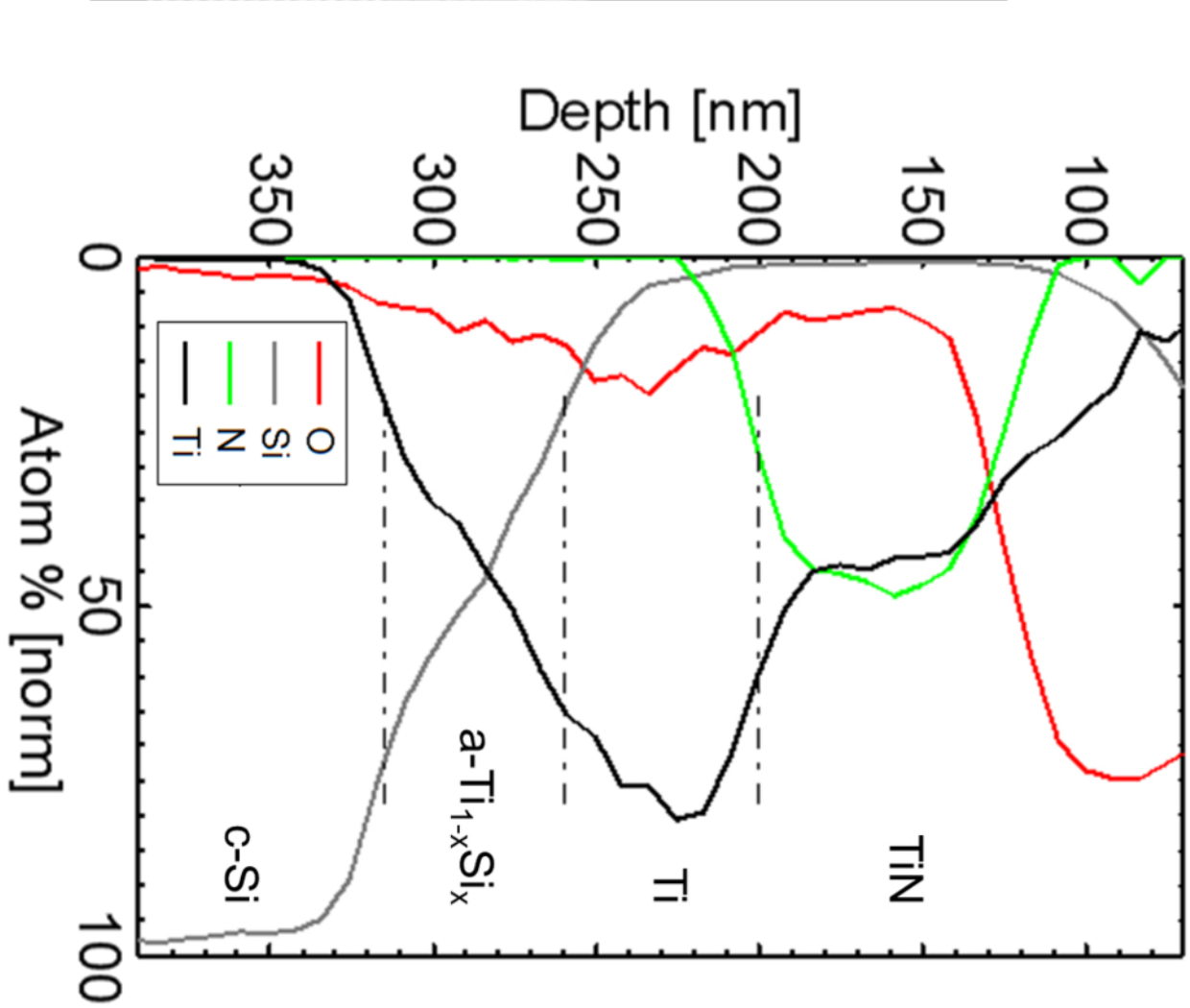

(b)

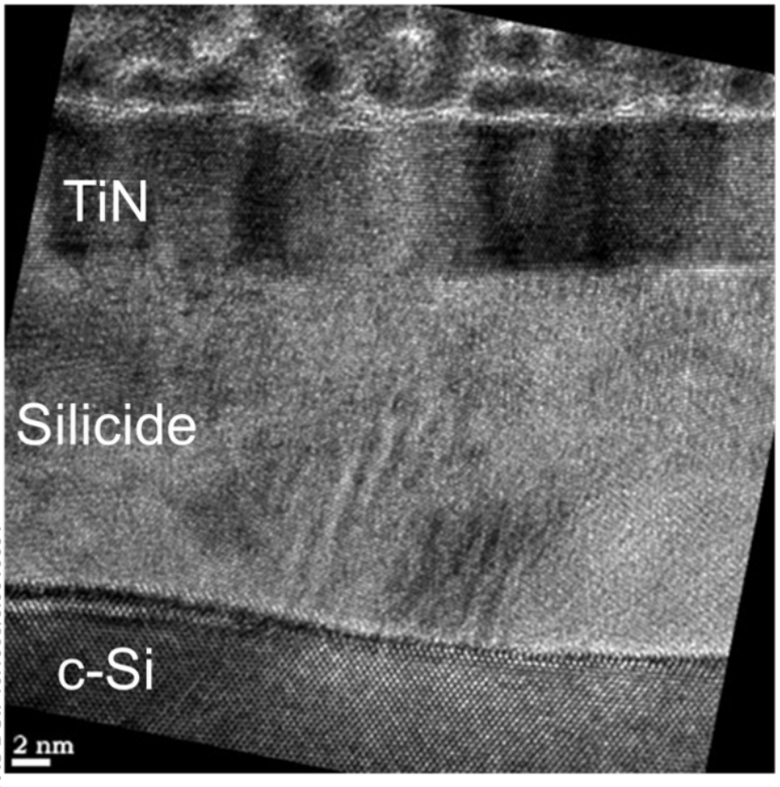

(a)

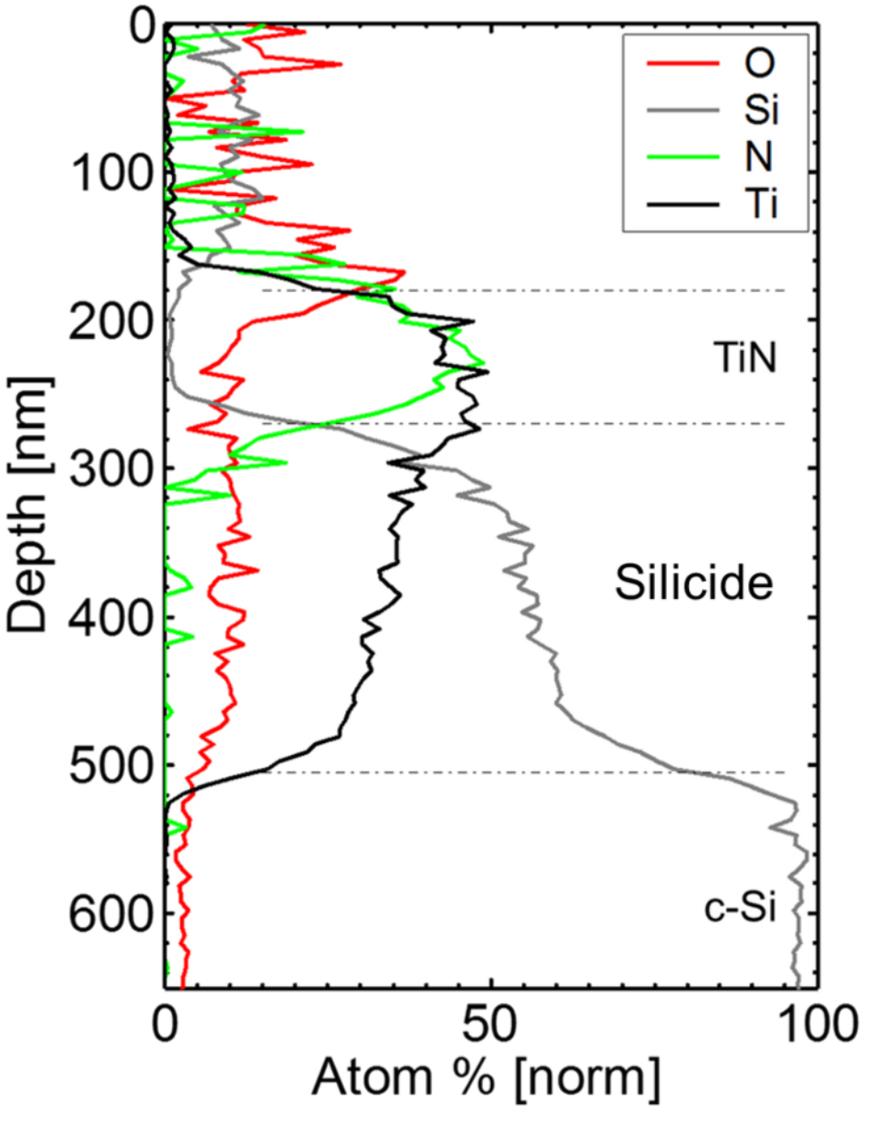

(b)

Journal of Applied Physics

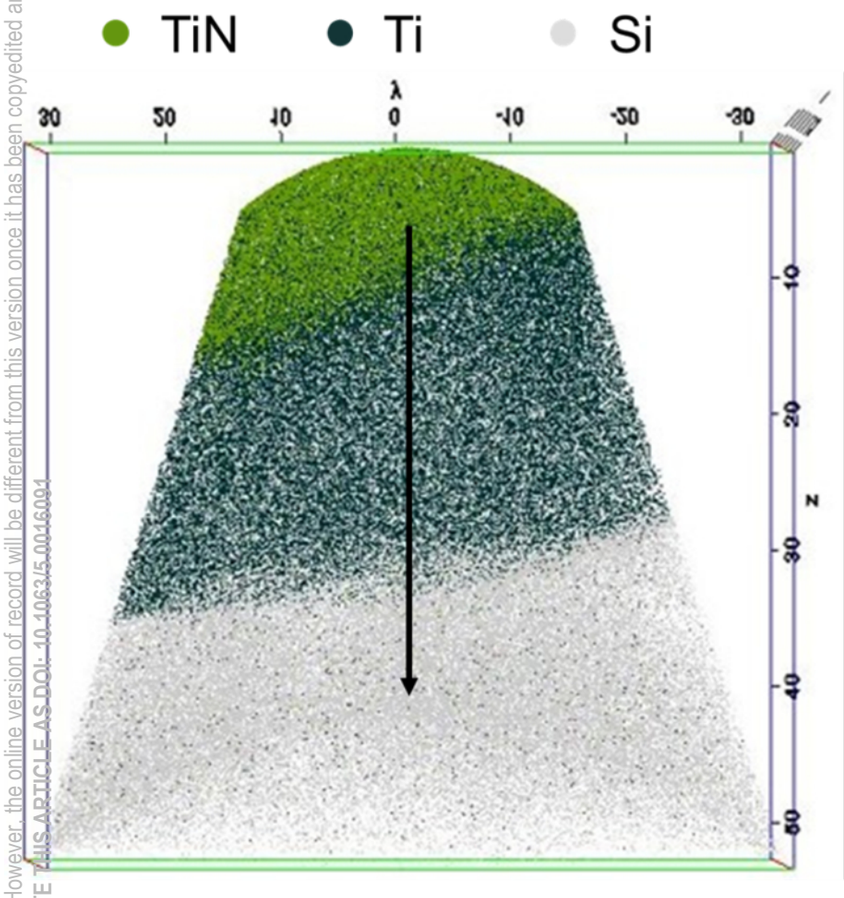

(a)

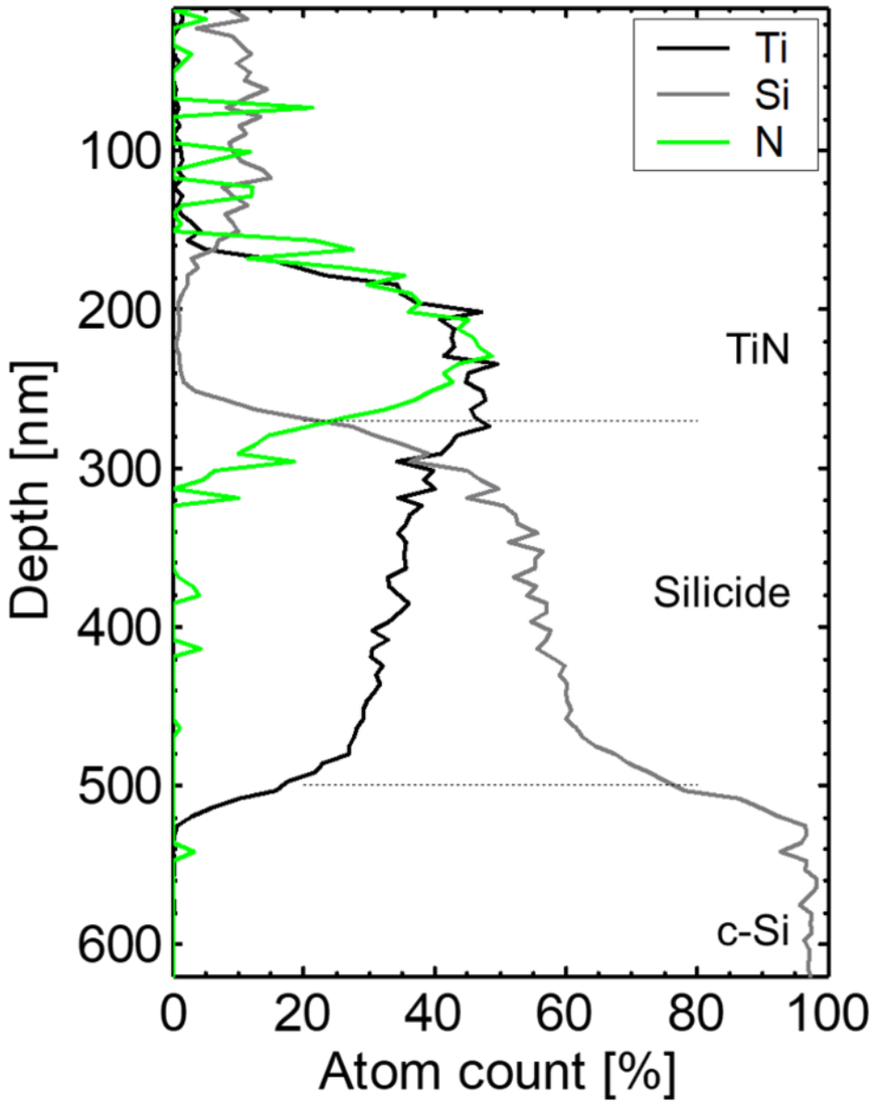

(b)

Journal of Applied Physics

AIP Publishing

AIP Publishing

Journal of Applied Physics

ACCEPTED MANUSCRIPT

PLEASE CITE THIS ARTICLE AS DOI: 10.1063/5.0016091

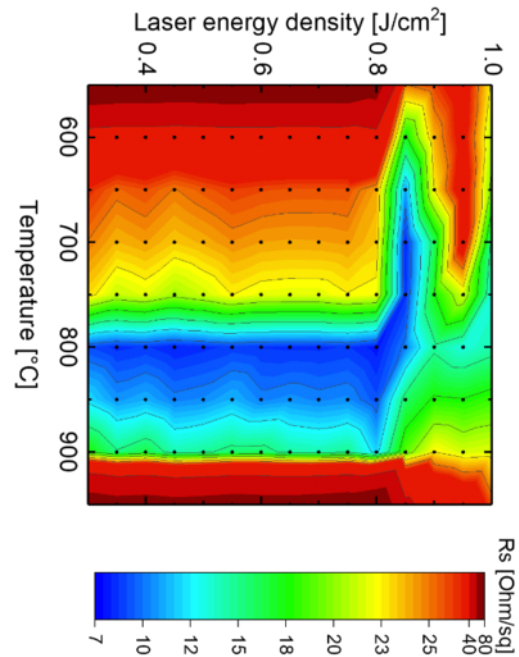

Journal of Applied Physics

Journal of Applied Physics

AIP Publishing
Journal of Applied Physics
ACCEPTED MANUSCRIPT

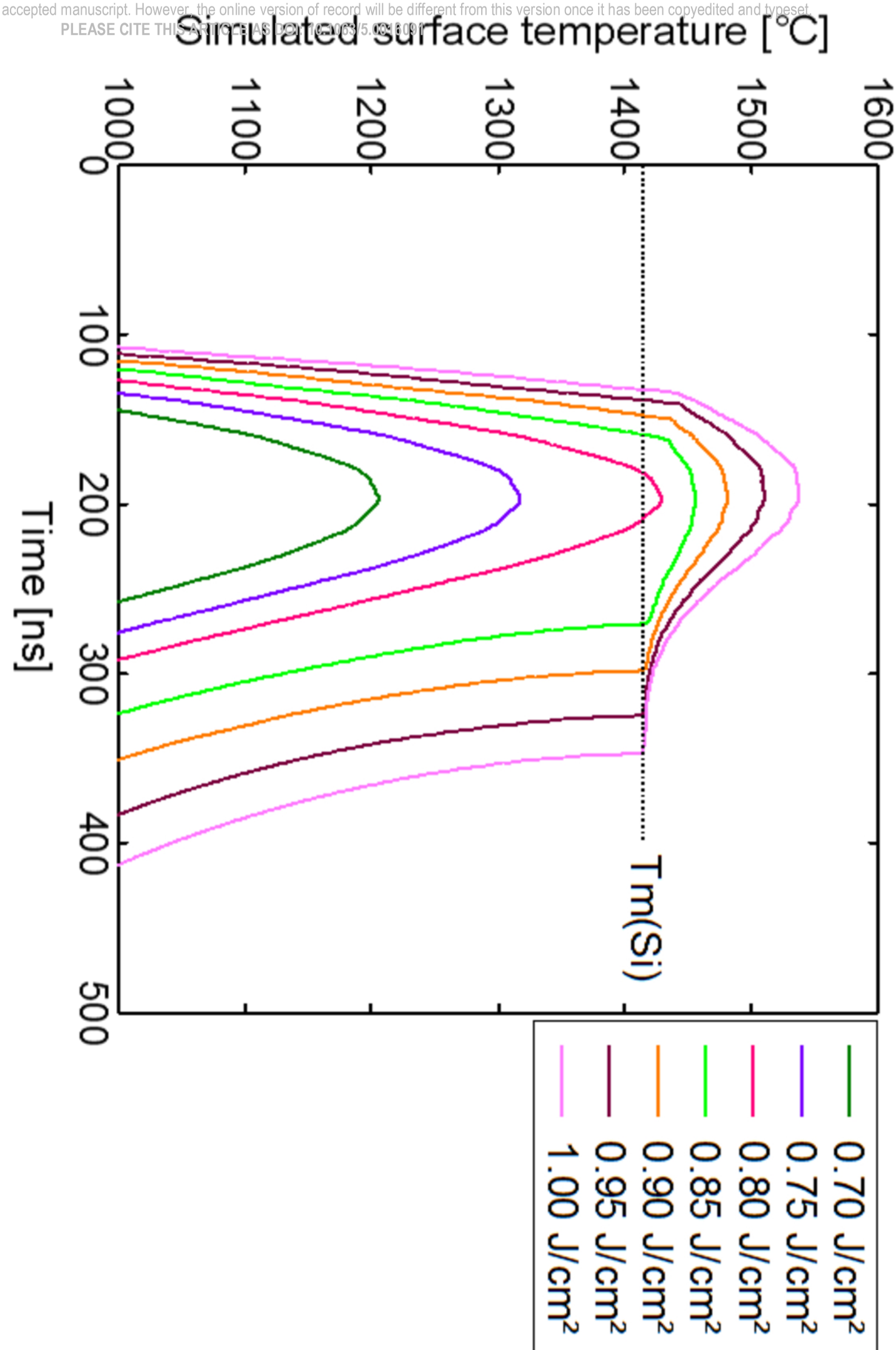

Journal of Applied Physics

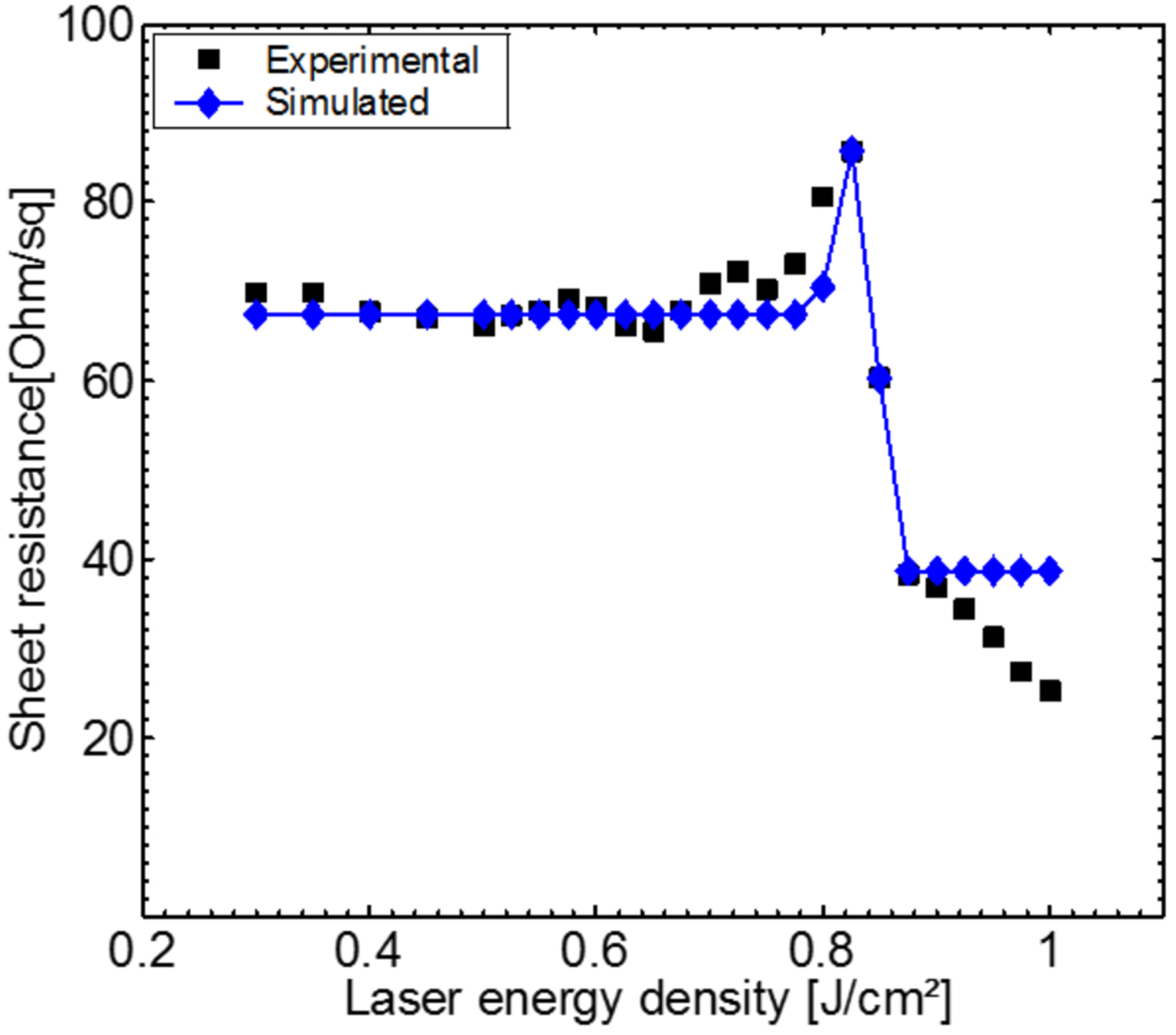

AIP Publishing

AIP Publishing

Journal of Applied Physics

ACCEPTED MANUSCRIPT

PLEASE CITE THIS ARTICLE AS DOI: 10.1063/5.0016091

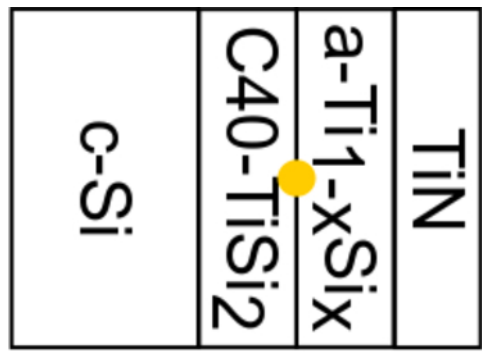

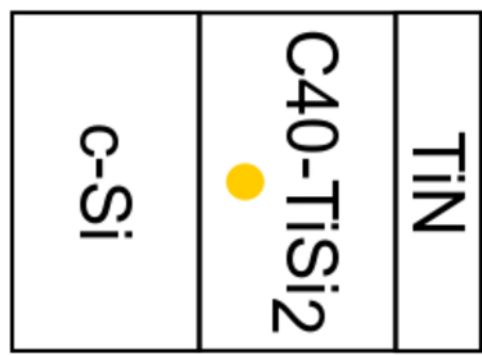

Journal of Applied Physics